Bulletin of Mathematical Biology (2020) 82:56
https://doi.org/10.1007/s11538-020-00731-0

Society for Mathematical Biology

ORIGINAL ARTICLE

Modeling Stripe Formation on Growing Zebrafish Tailfins

A. Volkening[1] · M. R. Abbott[2] · N. Chandra[3] · B. Dubois[3] · F. Lim[3] · D. Sexton[4] · B. Sandstede[3,5]

Received: 17 December 2019 / Accepted: 3 April 2020

Abstract
As zebrafish develop, black and gold stripes form across their skin due to the interactions of brightly colored pigment cells. These characteristic patterns emerge on the growing fish body, as well as on the anal and caudal fins. While wild-type stripes form parallel to a horizontal marker on the body, patterns on the tailfin gradually extend distally outward. Interestingly, several mutations lead to altered body patterns without affecting fin stripes. Through an exploratory modeling approach, our goal is to help better understand these differences between body and fin patterns. By adapting a prior agent-based model of cell interactions on the fish body, we present an in silico study of stripe development on tailfins. Our main result is a demonstration that two cell types can produce stripes on the caudal fin. We highlight several ways that bone rays, growth, and the body–fin interface may be involved in patterning, and we raise questions for future work related to pattern robustness.

Keywords Zebrafish · Pattern formation · Agent-based model · Tailfin · Self-organization · Growing domain

Mathematics Subject Classification 92

The work of A.V. has been supported in part by the National Science Foundation (NSF) through DMS-1148284, DMS-1764421, and DMS-1440386; by the Mathematical Biosciences Institute; and by the Simons Foundation/SFARI under 597491-RWC. M.R.A., N.C., B.D., F.L., and D.S. were supported by Brown University and ICERM through DMS-1439786. The work of B.S. was partially supported by the NSF through DMS-1408742 and DMS-1714429.

✉ A. Volkening
alexandria.volkening@northwestern.edu

1 NSF–Simons Center for Quantitative Biology, Northwestern University, Evanston, IL, USA

2 Mathematics, Statistics, and Computer Science, Macalester College, St. Paul, MN, USA

3 Division of Applied Mathematics, Brown University, Providence, RI, USA

4 Department of Mathematics, University of Idaho, Moscow, ID, USA

5 Data Science Initiative, Brown University, Providence, RI, USA

Published online: 30 April 2020

1 Introduction

A model organism with extensive biomedical applications, the zebrafish (*Danio rerio*) features black and gold stripes across its body and fins (see Fig. 1a). These namesake patterns emerge during development due to the interactions of pigment cells, which self-organize on the growing fish skin. Although it may seem natural for the same cell interactions to drive patterning across the fish, mutants (Fadeev et al. 2015) in which body patterns are altered, but fin stripes remain unchanged complicate this picture. The timeline of pattern development is also different on the body and the fins: Body stripes appear parallel to an existing horizontal marker (Frohnhöfer et al. 2013), but caudal fin patterns form outward during growth, raising questions about how horizontal alignment is specified there. To better understand these differences, here we develop an agent-based model of pigment cell interactions on growing tailfins.

Three main types of pigment cells make up zebrafish patterns: dark melanophores, orange/yellow xanthophores, and silver/blue iridophores. Until recently, the focus of the biological and mathematical communities was on the first two cell types, and a series of interactions taking the overarching form of short-range activation and long-range inhibition was identified (Nakamasu et al. 2009). This is a condition of Turing-type pattern formation (Turing 1952; Gierer and Meinhardt 1972); when it is invoked in zebrafish models, patterns are traditionally viewed as forming due to the reaction and diffusion of melanophores and xanthophores. In the last few years, however, new dynamics have surfaced, and it has become clear that iridophores play a critical role on the zebrafish body (Singh et al. 2014; Patterson and Parichy 2013; Singh and Nüsslein-Volhard 2015; Frohnhöfer et al. 2013). This is seen most strikingly in *shady*, a mutant that lacks iridophores and displays black spots across its body in place of stripes (Frohnhöfer et al. 2013; Lopes et al. 2008) (see Fig. 1b). Empirical studies (Singh et al. 2014; Patterson and Parichy 2013; Singh and Nüsslein-Volhard 2015) have shown that iridophores lead patterning and instruct the other cells on the fish body. Affirming this in silico, the two-cell model (Volkening and Sandstede 2015) could not produce complete body stripes without accounting for iridophores indirectly. These discoveries have led to active debate (Mahalwar et al. 2014; Singh et al. 2015; Watanabe and Kondo 2015a), as researchers work to reconcile the previous picture of two cell populations with new data about iridophores.

As we show in Fig. 1b, although *shady* fish develop spots on their bodies, the stripe patterns on their fins remain unchanged (Frohnhöfer et al. 2013). This raises several questions, and one immediately wonders why melanophores and xanthophores alone are incapable of producing stripes on the body, yet are sufficient on the fins. One possible explanation is that their interactions are intrinsically different in these two regions. Opinions on this diverge (Nüsslein-Volhard and Singh 2017; Singh et al. 2015; Singh and Nüsslein-Volhard 2015), with some researchers hypothesizing that melanophores and xanthophores behave largely the same in both domains (Watanabe and Kondo 2015b, a). It is also possible that different cell precursors or microenvironments are at work on the body and tailfin (Parichy and Spiewak 2015).

In addition to differences in the types of pigment cells involved in pattern formation on the body and tailfin, the timelines of pattern development in these regions are different. As we show in Fig. 2a, body stripes form sequentially outward from a central

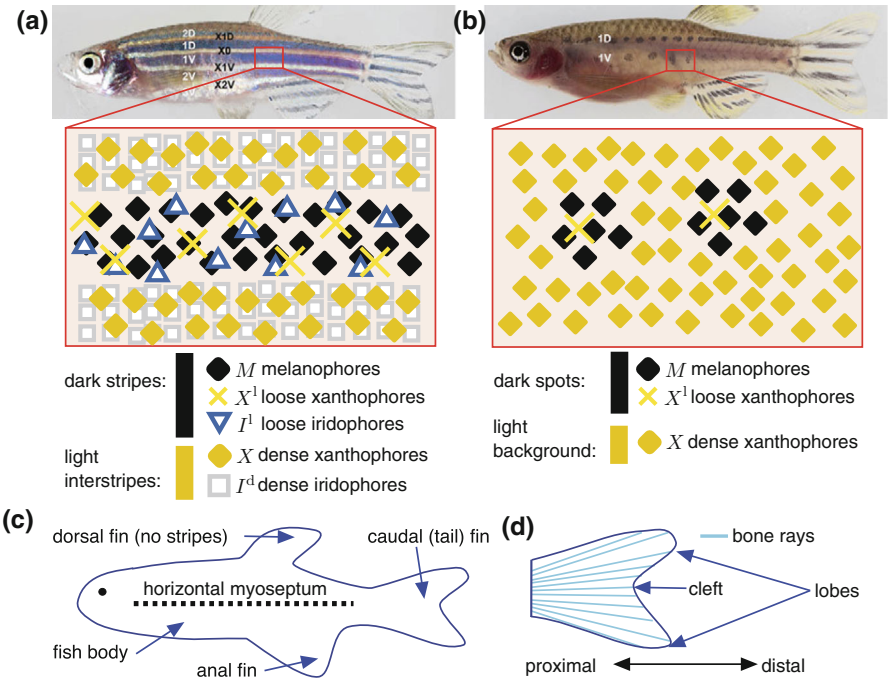

Fig. 1 Motivation and notation. **a** Wild-type zebrafish feature stripes across their bodies, as well as on their anal and caudal fins. Dark stripes consist of melanophores, loose xanthophores, and loose iridophores; and light stripes are made up of dense xanthophores and dense iridophores (Frohnhöfer et al. 2013; Hirata et al. 2005). For the remainder of this paper, we follow the empirical convention of calling light stripes "interstripes" and dark stripes "stripes." **b** The *shady* mutant (encoding ltk) lacks iridophores (Frohnhöfer et al. 2013; Lopes et al. 2008). While spots form on the bodies of these mutant fish, their fin patterns remain largely unchanged (Frohnhöfer et al. 2013). Although we show *shady* with dense and loose xanthophores as in the model (Volkening and Sandstede 2018), this is a simplification as *shady* xanthophores seem to be in an intermediate form (Mahalwar et al. 2016). **c**–**d** Here, we overview the fish notation relevant to our study. Fish images in (**a**) and (**b**) are reproduced with adaption from Frohnhöfer et al. (2013), licensed under CC-BY 3.0 (https://creativecommons.org/licenses/by/3.0/), and published by The Company of Biologists, Ltd; we added the red boxes and cell schematics (Color figure online)

strip of iridophores at the horizontal myoseptum. Loss of the horizontal myoseptum in the *choker* mutant leads to labyrinth patterns (Frohnhöfer et al. 2013). Similarly, disrupting the initial strip of cells in Fig. 2a through ablation produces patterns with lost directionality (Patterson and Parichy 2013; Yamaguchi et al. 2007). The horizontal myoseptum therefore specifies initial alignment on the body and, by spreading ventrally and dorsally from this marker, iridophores provide further directionality cues (Singh et al. 2014). Body stripes then emerge sequentially outward from the fish center in a direction parallel to established stripes (see Fig. 2b). In contrast, as we note in Fig. 2c, tailfin stripes grow from proximal to distal [e.g., see images of fin development in Parichy et al. (2009)]; proximal-to-distal patterning has also been noted after tailfin amputation (Rawls and Johnson 2000; Eom et al. 2015). Although new stripes are added dorsally and ventrally, they seem to develop by gradually extending in a

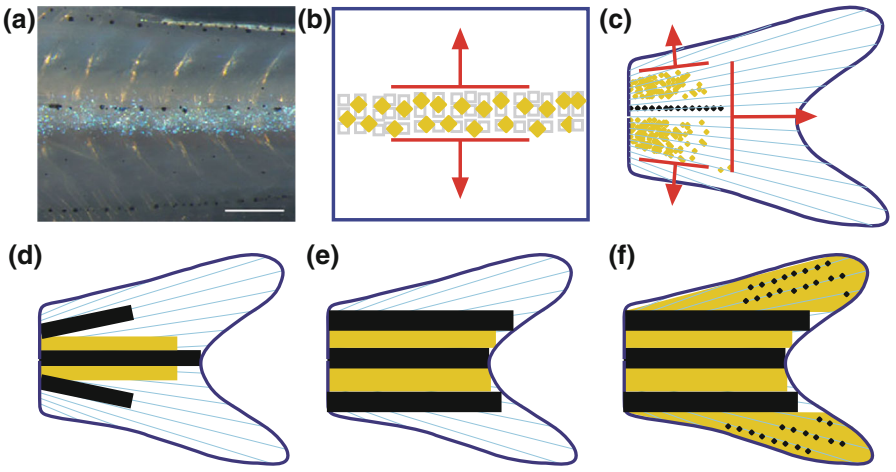

Fig. 2 Differences in pattern formation on the body and tailfin. **a** On the zebrafish body, iridophores emerge along the horizontal myoseptum to create the first interstripe (Singh et al. 2014; Singh and Nüsslein-Volhard 2015). **b** The strip of iridophores at the horizontal myoseptum provides an initial source of alignment, and stripes form sequentially in parallel to this marker (Frohnhöfer et al. 2013). **c** In contrast, new stripes on the tailfin form by slowly extending from the proximal to the distal edge, so that the direction of pattern growth is roughly perpendicular to the developing stripes (Tu and Johnson 2010). **e–f** Based on our observations of empirical images in Parichy et al. (2009), stripes initially develop radially (e.g., in association with the bone rays), before adopting a more horizontal alignment on the tailfin. **f** The presence of melanophores aligned with the bone rays is particularly pronounced in the fin lobes [our observation based on images in Parichy et al. (2009)]. Image (a) is reproduced from Frohnhöfer et al. (2013), licensed under CC-BY 3.0 (https://creativecommons.org/licenses/by/3.0/), and published by The Company of Biologists, Ltd

direction roughly perpendicular to the stripes on the tailfin. Moreover, as we illustrate in Fig. 2d and e, stripes initially appear radially along the bone rays, but later adopt a horizontal alignment [our observation based on images in Parichy et al. (2009)]. The presence of melanophores along the bones (illustrated schematically in Fig. 2f) is particularly pronounced in the lobes [e.g., Fig. 13 in Parichy et al. (2009)].

While much work has been done to identify cell dynamics on the zebrafish body, there are fewer results focused specifically on uncovering pigment cell behaviors on the fins. On the empirical side, melanophores and xanthophores extracted from fins have been used in in vitro experiments (Yamaguchi et al. 2007; Inaba et al. 2012; Inoue et al. 2014; Watanabe et al. 2016). Tu and Johnson (2010) have studied melanophore lineages, precursors, and spreading on fins. Additionally, Parichy et al. (2009) provide images of stripe formation on zebrafish as a whole. The tailfin is amenable to amputation, and the studies (Goodrich and Nichols 1931; Kizil et al. 2009; Tu and Johnson 2011; Rawls and Johnson 2000; Pfefferli and Jaźwińska 2015; Goodrich et al. 1954) involved amputating the fin and observing regrowth. Furthermore, several works (e.g., Mills et al. 2007; Quigley et al. 2005; Iwashita et al. 2006; Mellgren and Johnson 2006; Parichy and Turner 2003; Eom et al. 2012) discuss the impact of mutations on the fins of zebrafish or other *Danio*s. Prior mathematical studies (Bullara and De Decker 2015; Gaffney and Lee 2015; Woolley et al. 2014; Bloomfield et al. 2011; Painter et al. 2015; Caicedo-Carvajal and Shinbrot 2008; Moreira and Deutsch 2005;

Nakamasu et al. 2009; Volkening and Sandstede 2015, 2018), however, have either focused on the zebrafish body or made no attempt at differentiating between the body and the fins.

Studying the tailfin is an important problem from the perspective of zebrafish-pattern research because it would provide a more cohesive understanding of pigment cell interactions (Kondo and Watanabe 2015; Singh and Nüsslein-Volhard 2015). The ability of tailfin patterns to regenerate after amputation also suggests potential applications to wound healing and tissue regeneration (Parichy and Spiewak 2015). We therefore put forward an initial modeling step toward a more comprehensive view of zebrafish stripes here. Our objective is twofold:

(1) To help elucidate whether there are necessarily differences in the cell interactions underlying pattern formation on the body and tailfin of zebrafish; and
(2) To help determine whether patterns can arise autonomously due to melanophore and xanthophore interactions or whether external cues are needed to align stripes on the tailfin.

Based on experimental observations that iridophores are not involved in stripe formation on the caudal fin (Watanabe and Kondo 2015b), we approach this problem by adapting the prior melanophore–xanthophore body model (Volkening and Sandstede 2015) on growing tailfin domains. This model has the overarching form of short-range activation and long-range inhibition (Turing 1952; Gierer and Meinhardt 1972), and it allows us to test if the same melanophore and xanthophore interactions can account for stripe formation on the body and tailfin. We test the body model (Volkening and Sandstede 2015) on caudal-fin domains under different mechanisms of epithelial growth and extend it to account for fin-specific dynamics. Our model suggests that melanophores and xanthophores can produce stripe patterns on the tailfin without iridophores, but additional mechanisms may be needed to ensure stripes form robustly. We find that epithelial growth and bone rays may provide directionality cues, serving as a means of reconciling differences between body and fin patterns on zebrafish.

Regarding manuscript organization, we begin in Sect. 2 by motivating and identifying a series of proposed mechanisms that may be involved in pattern formation on the caudal fin. We then present our models of tailfin growth and cell interactions in Sect. 3. By simulating our agent-based model on growing fin domains in Sect. 4, we test how skin growth, the body–fin interface, and the presence of bone rays may affect stripe formation and alignment on the tailfin. We conclude in Sect. 5 by summarizing our study and highlighting directions for future work. We include all of our model parameters and detailed simulation conditions in "Appendices A and B."

2 Proposed Mechanisms of Pattern Formation on the Tailfin

To gain some intuition into what instructs stripe patterns to form on the tailfin without iridophores, it is useful to compare the timelines of development on the body and caudal fin. As we illustrate in Fig. 2a and b, stripes and interstripes develop sequentially in directions dorsal and ventral to a horizontal marker on the fish body (Frohnhöfer et al. 2013). In particular, narrow stripes emerge parallel to the horizontal myoseptum across

the full length of the body, and then these stripes widen in time. In contrast, stripes and interstripes gradually develop by spreading from proximal to distal across the caudal fin. (The boundary of un-patterned space is parallel to stripes on the body, but it is perpendicular on the tailfin.)

Disparate types of epithelial growth on the body and tailfin could potentially explain the differences in pattern development between these two regions. While the skin on the fish body grows uniformly, tailfin growth occurs distally through the addition of new bone segments at ray tips (Watanabe and Kondo 2015b; Goldsmith et al. 2003; Iovine and Johnson 2000; Iovine 2007). It has been hypothesized that such ray growth could be a source of directionality on the tailfin (Watanabe and Kondo 2015b). Unlike on the body, however, it is less clear what kind of epithelial growth occurs on the fins (Goldsmith et al. 2003). If skin and bone growth are both limited to the distal edge, skin cells would differentiate in the fin lobes in response to the addition of new bone-ray segments. In this setting, pigment cell positions would not be altered by skin growth, and stripe alignment could be specified by the controlled appearance of empty space at the distal edge (see Fig. 4a). Alternatively, under uniform epithelial growth like that present on the body, skin cells would constantly differentiate across the fin (see Fig. 4b). Cell positions would evolve as if they were sitting on an expanding rubber sheet, providing an alternative source of radial directionality. Notably, in the work (Tu and Johnson 2010), Tu and Johnson tracked melanophore lineages across the caudal fin. They found that most new melanophores are added in the distal third of the developing stripes (though they also observed some melanophore birth across the entire pattern). These findings (Tu and Johnson 2010) could be accounted for by a combination of uniform and distal epithelial growth, for example.

Although the simplest explanation for patterning on the caudal fin may be that skin growth steps in to specify stripe alignment and fill the role of iridophores on the body, empirical images of fins in Parichy et al. (2009) point to a few features of cell organization that complicate this hypothesis. [We note that we cannot republish images from Parichy et al. (2009), but we describe them here and refer the reader to this reference for fin images.] First, the radial nature of melanophore organization on the tailfin is noticeable by eye: melanophores appear dispersed along the bones, particularly in the lobes (see Fig. 2d, f). As the fish develops, stripes gradually spread across the fin, initially radially, but later adopting a parallel arrangement (see Fig. 2d–f). The intermingling of melanophores and xanthophores (Eom et al. 2015) in the lobes stands out, and it is unclear how to reconcile these dynamics with the local competition observed between these cells on the body (Nakamasu et al. 2009; Takahashi and Kondo 2008). Lastly, we do not know whether any cell interactions occur across the proximal boundary, where the body and fin connect. It is possible that cells enter the tailfin from the body, providing a proximal source of cells and alignment cues from the body pattern [e.g., the early study (Goodrich et al. 1954) suggested that xanthophore precursors could conceivably enter the caudal fin from the body].

There are multiple mechanisms that could explain the apparent radial organization of melanophores on the tailfin. Bone rays could physically corral cells and affect their movement, especially where the fin is thinnest near the lobes. Alternatively, melanophores may differentiate from precursors associated with or between the rays. For example, Tu and Johnson (2010) showed that the boundaries of melanophore-clone

distributions in the tailfin are parallel to the bone rays. In an early study (Goodrich et al. 1954), melanophores were observed as entering interstripes along fin rays on the anal fin. In this case, bones could serve as an external source of directionality on the tailfin like the horizontal myoseptum does on the body. The initially radial, later horizontal, development of stripes could be related to fin thickness or be explained by an additional signal spreading from proximal to distal on the tailfin. Finally, it is conceivable that the melanophores that we observe along the rays in images from Parichy et al. (2009) are in a larval (e.g., inactive) form and are later replaced by adult cells. The presence of distinct classes of melanophores on the fins has been noted by several studies (e.g., Tu and Johnson 2010; Rawls and Johnson 2000).

To put some delimiters on the realm of possible processes at work on the tailfin, we test the following mechanisms for wild-type pattern development:

I Distal epithelial growth (Fig. 4a);
II Alignment cues from body patterns (Fig. 4g);
III Uniform epithelial growth along bone rays (Fig. 4b);
IV Melanophore migration along bone rays (Fig. 4e); and
V Melanophore differentiation in association with bone rays (Fig. 4h).

In all cases, we consider the interactions of two cell types (melanophores and xanthophores) on growing tailfin domains. To implement Mechanisms I–V, we introduce a model of cell interactions that includes switch parameters (see Sect. 3). By setting our switch parameters to extreme values (e.g., -1 or 1000 cells), we select the mechanisms that we include in a given simulation.

3 Model

On the caudal fin, stripes are made up of a layer of xanthophores sandwiched between two sheets of melanophores, and interstripes contain a sheet of xanthophores (Hirata et al. 2005). Although fins also contain iridophores, they do not match up with the stripes like on the body (Watanabe and Kondo 2015b). Recent work (Mahalwar et al. 2014; Walderich et al. 2016) has shown that body xanthophores appear in fundamentally different forms in stripes and interstripes, and we expect that a similar distinction is present on the tailfin. In this first model of fin patterns, we therefore take a minimal approach and consider a single layer of cells, with black melanophores (M) in stripes and gold dense xanthophores (X) in interstripes.

We base our model for cell interactions on a prior model (Volkening and Sandstede 2015) of M and X cells on the zebrafish body. We use an agent-based approach, modeling cells as point masses that undergo deterministic migration (by coupled ordinary differential equations) and stochastic birth and death (through noisy, discrete-time rules). In particular, we let

$$\begin{aligned}
\mathbf{M}_i(t) &= \text{position of the center of the } i\text{th melanophore at time } t,\\
\mathbf{X}_j(t) &= \text{position of the center of the } j\text{th xanthophore at time } t,\\
N_{\mathrm{M}}(t) &= \text{number of melanophores at time } t, \text{ and}\\
N_{\mathrm{X}}(t) &= \text{number of xanthophores at time } t,
\end{aligned}$$

where we measure time in days. The number of cells on the fin grows in time, varying from roughly 250 to 5000 cells over the course of one of our simulations.

We track the full tailfin domain, with its growing shape determined by tracing curves around images in Parichy et al. (2009) and interpolating between these curves. Using images in Parichy et al. (2009), we also specify bone rays on our domains. To test how the presence of bones may affect pattern formation (namely Mechanisms III–V in Sect. 2), we discretize the bone rays as below:

$$\{\mathbf{B}_i^j(t)\}_{i=1,\ldots,500} = \text{ set of coordinates for the } j\text{th discretized bone ray at time } t, \tag{1}$$

where the initial coordinate of each discretized bone is along the y-axis and the discretization step in the x-direction is $\Delta b_x = x_{\max}(t)/499$ (as we show in Fig. 3, $x_{\max}(t)$ is the length of the caudal fin at time t days). (When we plot bones in our simulations, we only show the discretized bone coordinates that fall within our tailfin domains.) We use the same number of discretization points per bone regardless of fin size; in future models, one could alternatively keep Δb_x constant in time.

We simulate pattern development from when zebrafish are roughly 18 days post-fertilization (dpf) to when they reach adult stages at 150 dpf. It is important to note that growth rates vary in vivo, and experimentalists prefer to track time using developmental stage or a measure of body length called standardized standard length (SSL) (Parichy et al. 2009). Generally reported without units (McMenamin et al. 2016), SSL is a measurement of standard length (SL) in mm based on representative zebrafish; see Fig. 3a. To follow conventions and account for broad audiences, we track time using both developmental stage and time in dpf (see Sect. 3.1 for details). We provide our relationships between SSL, developmental stage, and time in Table 1.

In the following subsections, we describe our model of growing fin domains (Sect. 3.1) and then introduce our agent-based model of cell interactions, adapted from the body model (Volkening and Sandstede 2015) (Sect. 3.2). For a summary of our model, see Fig. 4. We include further details about our simulations and parameters for reproducibility in "Appendices A and B."

3.1 Model of Growing Tailfin Domains

Because it contains many caudal fin images, we draw heavily on the work (Parichy et al. 2009) to specify the shape, bone-ray placement, and growth rates for our domains. In particular, we manually sharpen seven caudal-fin images from Parichy et al. (2009) using Adobe Photoshop, identify the (x, y)-coordinates of the fin boundaries in the cleaned images using Matlab, and smooth any rough edges in the resulting curves. As

Table 1 Stages of development, estimated fish age, and fin images

Stage	SSL	Estimated age	Fin image in Parichy et al. (2009)
Pelvic fin bud (PB)	7.2	18 dpf	Fig. 47G'
Pelvic fin ray (PR)	8.6	24 dpf	Fig. 49G'
Squamation onset posterior (SP)	9.8	33 dpf	Fig. 51G'
Juvenile (J)	11.0	43 dpf	Fig. 53G'
Juvenile+ (J+)	13.0	70 dpf	Fig. 54G'
Juvenile++ (J++)	16.0	93 dpf	Fig. 55E'
Adult (A)	26	278 dpf	Fig. 56E'

As we show in Fig. 3a, SL is a measurement of fish body length (not including the caudal fin). SSL is a characteristic SL based on representative zebrafish (Parichy et al. 2009). SSL is conventionally not reported with units (McMenamin et al. 2016), but it is associated with SL measured in mm. To produce our growing domains, we trace fin boundaries in fish images from Parichy et al. (2009). We estimate age from SSL using Eq. (3)

we note in Table 1, these fin images span from 7.2 SSL to 26 SSL. To approximate the fish age and specify scale bars for each image, we convert these SSL (body length) measurements to HAA (body height) measurements as follows:

$$\text{HAA} = 0.259 \times \text{SSL} - 0.985 \text{ mm}, \tag{2}$$

where this relationship is our approximation from figures in Parichy et al. (2009). Based on images in Parichy et al. (2009), we then estimate the height of the tailfin at its proximal boundary as roughly equal to 70% of the fish body height (that is, our fin base height $= 0.7 \times$ HAA). See Fig. 3a. To approximate the age of the fish in each image, in turn, we relate SSL and time below:

$$\text{time in dpf} = \begin{cases} \exp\left(\frac{4.8291+\text{SSL}}{4.1994}\right) & \text{if time} \leq 85 \text{ dpf} \\ \frac{10.949+\text{SSL}}{0.0541} & \text{if time} > 85 \text{ dpf} \end{cases}, \tag{3}$$

where this relationship is our approximation based on graphs in Parichy et al. (2009). Through this process, we assign a spatial scale and time stamp (in dpf) to each of our traced caudal-fin images (see Table 1). To span the time between our seven images, we calculate a boundary curve for each day of simulated development by assuming linear growth and a continuous transformation to each new image.

In addition to defining the outline of our fin domains, we add bone rays each day. Based on the images that we gathered from Parichy et al. (2009), we estimate that the angle between consecutive bone rays is roughly 2.5°–4.5°, decreasing with zebrafish age (Fig. 3b). We specify bone rays at a constant 2.833° apart, and, motivated by Rolland-Lagan et al. (2012), Iovine (2007) and Goldsmith et al. (2006), we include 18 rays on our domain. Each day we define the bones in five steps:

1. Find the coordinates of the upper and lower endpoints of the proximal boundary of the fin, namely $(0, y_{\max}(t))$ and $(0, y_{\min}(t))$.
2. Define $y_{\text{avg}} = \frac{y_{\max(t)}+y_{\min(t)}}{2}$.

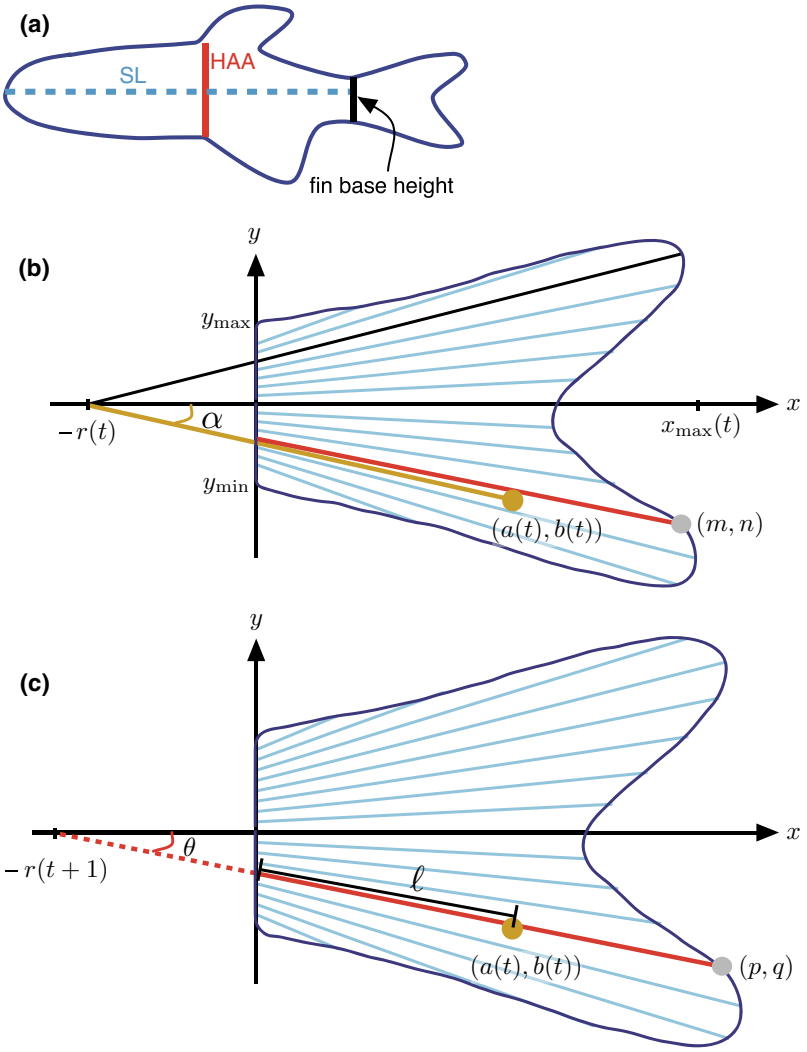

Fig. 3 Fin domain and growth. **a** We develop our growing domain by tracing images of fins and bone rays in Parichy et al. (2009); also see Table 1. To determine the right spatial scaling for these images, we use the SSL reported in Parichy et al. (2009) for each image. By relating this SSL to measurements of body length (SL) and height (HAA), we estimate the height of the fin at its proximal edge (see Eq. 2). The height that we estimate for the fin base provides the necessary scaling information for our domains. **b** and **c** When we include uniform epithelial growth (Mechanism III in Sect. 2), we scale cell positions in time with bone growth; also see Fig. 4b. For example, to adjust the position of the cell at position $\mathbf{X}_i(t) = (a(t), b(t))$, we first identify the scaling angle (α) and the rays (highlighted in red) that are closest to $\mathbf{X}_i(t)$ in the current fin domain at day t and the next fin domain at day $t+1$. To determine the amount to scale in the direction α, we calculate how much the nearest rays grow between these two days. Here, (m, n) and (p, q) are the endpoints of the closest rays to $(a(t), b(t))$ at day t and $t+1$, respectively. Moreover, $\ell \approx \left|\frac{a(t)}{\cos(\theta)}\right|$; we note that this is generally not a strict equality because we define $-r(t+1)$ to be the position where the third most dorsal bone at day $t+1$ intersects the x-axis, and the bones do not all intersect the x-axis at exactly the same point (see Sect. 3.1 for details)

3. Calculate the limits of ray placement by shrinking the interval slightly so that bones do not emanate directly from the upper and lower boundary of the domain.

$$y_{\max}^{\text{bone}} = (y_{\max}(t) - y_{\text{avg}}) \times 0.95 + y_{\text{avg}},$$
$$y_{\min}^{\text{bone}} = (y_{\min}(t) - y_{\text{avg}}) \times 0.95 + y_{\text{avg}}.$$

4. Discretize the proximal fin boundary into 18 equidistant points between $(0, y_{\max}^{\text{bone}}(t))$ and $(0, y_{\min}^{\text{bone}}(t))$.
5. Define rays emanating from each of these points at angles ranging from 25.5° to −22.667° with a step of 2.833°.

In some simulations, we include uniform epithelial growth (Mechanism III in Sect. 2), and so we scale cell positions with bone growth (see Fig. 4a, b). For a given cell, we implement this by first identifying the direction in which we will scale the cell coordinates and then determining the scaling factor that we will apply (see Fig. 3b, c). We make the simplifying assumption that each day all the rays intersect at the same point $(-r(t), 0)$. We define this point $(-r(t), 0)$ to be the place where the third most dorsal ray (highlighted in black in Fig. 3b) crosses the x-axis. In particular, for a cell with coordinates $(a(t), b(t))$ at time t, its scaling angle α is

$$\alpha = \text{ scaling angle } = \text{ atan}\left(\frac{b(t)}{a(t) + r(t)}\right).$$

We then calculate the cell's scaling factor by finding its nearest bone rays at time t and $t + 1$ days (e.g., they have endpoints (m, n) and (p, q) in the example in Fig. 3b, c):

$$S = \text{scaling factor} = \frac{\text{length of closest ray to } (a(t), b(t)) \text{ at time } t + 1}{\text{length of closest ray to } (a(t), b(t)) \text{ at time } t}.$$

We estimate ray length using the discretized bone points in Eq. (1) that fall within our domain. Lastly, we update the coordinates of the cell at $(a(t), b(t))$ as below:

$$a(t) = S\left|\frac{a(t)}{\cos(\theta)}\right|\cos(\alpha),$$
$$b(t) = (S - 1)\left|\frac{a(t)}{\cos(\theta)}\right|\sin(\alpha) + b(t),$$

where $\theta = \text{ atan}\left(\frac{q}{p+r(t)}\right)$ is the angle that the closest ray to the pigment cell on the updated domain makes with the x-axis. We note that $\left|\frac{a(t)}{\cos(\theta)}\right| \approx \ell$ in Fig. 3c.

3.2 Model of Cell Interactions

Pigment cells on the skin of zebrafish interact locally with neighboring cells [e.g., through direct contact (Walderich et al. 2016) or short dendrites (Inaba et al. 2012)]

and at long range with cells in neighboring stripes (Nakamasu et al. 2009). Long-range interactions may be mediated by cellular extensions, such as airnemes or pseudopodia, which have been measured to be up to half a stripe width in length (Eom et al. 2015; Hamada et al. 2014). Diffusion of signaling factors may also play a role (Patterson et al. 2014). We account for these various length scales (see Fig. 4c) with four interaction neighborhoods:

$$\Omega^{\mathbf{z}}_{\text{podia}} = \text{annulus of inner radius 318 } \mu\text{m and width 25 } \mu\text{m centered at } \mathbf{z}, \tag{4}$$

$$\Omega^{\mathbf{z}}_{\text{rand}} = \text{disk centered at } \mathbf{z} \text{ with radius } \Delta_{\text{rand}} = 100\ \mu\text{m}, \tag{5}$$

$$\Omega^{\mathbf{z}}_{\text{crowd}} = \text{local overcrowding disk centered at } \mathbf{z} \text{ with radius } \Delta_{\text{XM}} = 82\ \mu\text{m, and} \tag{6}$$

$$\Omega^{\mathbf{z}}_{\text{loc}} = \text{short-range disk of radius } d_{\text{loc}} \in \{75, \Delta_{\text{XM}}\}\ \mu\text{m centered at } \mathbf{z}, \tag{7}$$

where Δ_{XM} is the average distance between M and X cells at stripe–interstripe boundaries (Takahashi and Kondo 2008). Our rules for cell interactions depend on the proportions of cells in these neighborhoods. We implement this by introducing indicator functions that identify whether or not a cell is in a neighborhood around the point $\mathbf{z}$:

$$\mathbb{1}_{\Omega^{\mathbf{z}}_{\text{region}}}(\mathbf{C}) = \begin{cases} 1 & \text{if position } \mathbf{C} \text{ lies within the region centered at } \mathbf{z} \\ 0 & \text{otherwise} \end{cases}, \tag{8}$$

where region $\in$ {podia, rand, crowd, loc}. We note that Ω_{podia}, Ω_{rand}, and Ω_{crowd} are the same regions used in the body model (Volkening and Sandstede 2015). As discussed there, Ω_{podia} accounts for cell interactions across half a stripe width in distance. In Volkening and Sandstede (2015), $d_{\text{loc}} = 75\ \mu$m for Ω_{loc}, but we increase this parameter slightly to Δ_{XM} in some of our fin simulations (see "Appendix B.5").

In the next subsections, we describe how we adapt the model (Volkening and Sandstede 2015) to account for cell movement (Sect. 3.2.1), differentiation (Sect. 3.2.2), and competition (Sect. 3.2.3) on the caudal fin. For details about the order in which we implement these interactions, see "Appendix B.1." Briefly, we implement $1/\Delta t_{\text{mig,birth}}$ iterations of migration followed by birth; we then evaluate cells for possible death with a time step of $\Delta t_{\text{death}} = 1$ day; and finally, we implement skin growth with a time step of $\Delta t = 1$ day (note that $\Delta t_{\text{mig,birth}} \leq 1$ day). We provide all of our parameters in Tables 2, 3, and 4 in "Appendix A." With small adjustments in some simulations, these parameters are based on the prior body model (Volkening and Sandstede 2015).

3.2.1 Cell Migration

For each day of simulated development, we implement $1/\Delta t_{\text{mig,birth}}$ cycles of cell movement, where $\Delta t_{\text{mig,birth}} \leq 1$ day. We specify the movement of the ith X cell, located at position $\mathbf{X}_i(t)$, with the same first-order ordinary differential equation used in the prior body model (Volkening and Sandstede 2015), namely:

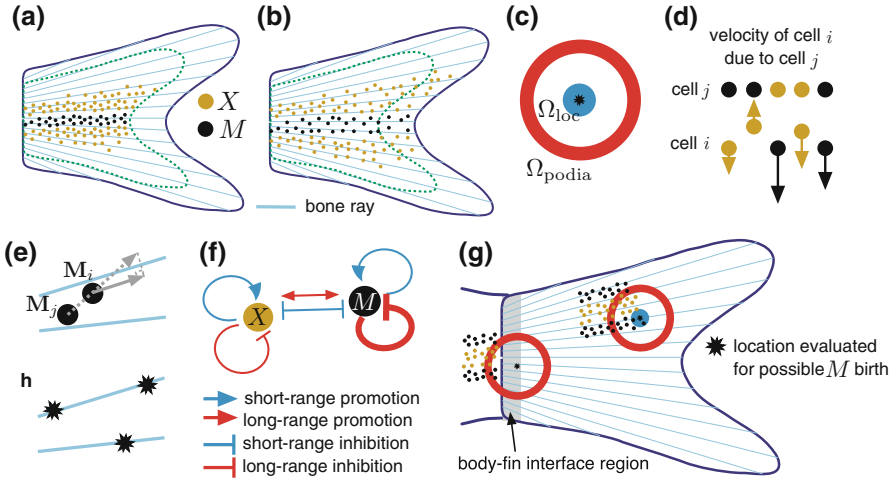

Fig. 4 Model overview. **a** Under the assumption of distal epithelial growth (Mechanism I in Sect. 2), we do not scale cell positions as the fin grows. The dashed green curve indicates the fin boundary at time t days and the solid blue curve denotes the boundary at $t + 1$ days. **b** In contrast, under uniform epithelial growth (Mechanism III), we scale cell positions along the rays with fin growth (see Fig. 3b, c and Sect. 3.1 for details). **c** Cell interactions depend on a combination of short- and long-range signals (Nakamasu et al. 2009). Using the same approach as Volkening and Sandstede (2015), we account for these interactions through stochastic rules that depend on the number of cells in a short-range disk (Ω_{loc}) and a long-range annulus (Ω_{podia}) around the cell (or precursor) of interest. **d** Similar to Volkening and Sandstede (2015), we specify repulsive and attractive forces between cells. The cell separation and arrow lengths in this schematic are not to scale, but capture qualitative features of cell migration (e.g., we indicate that X–X repulsion is weaker than M–M repulsion with a shorter velocity arrow). As we discuss in Sect. 3.2.1, in some simulations we remove the local attractive force from M cells on X cells. **e** Under Mechanism IV, we specify that M cells do not migrate across rays. To implement this for the cell at position $\mathbf{M}_i$, we find its velocity and then project this along its nearest bone. **f** Cell birth and death take the form of short-range activation and long-range inhibition in our model and Volkening and Sandstede (2015). **g** Under Mechanism II, we test how cells receiving alignment cues from developing body stripes may impact patterning. To do this, we adjust our rules for cell birth in a small (grey) neighborhood of the fin's proximal edge. In this neighborhood, we require that birth depends only on long-range signals. **h** To test how specifying M birth in association with the bones impacts pattering, we limit M birth to locations on the rays under Mechanism V

$$\frac{d\mathbf{X}_i}{dt} = -\sum_{j=1, j\neq i}^{N_{\text{X}}} \nabla Q^{\text{XX}}(\mathbf{X}_j - \mathbf{X}_i) - \sum_{j=1}^{N_{\text{M}}} \nabla Q^{\text{MX}}(\mathbf{M}_j - \mathbf{X}_i), \tag{9}$$

where the potentials Q^{pq}, which describe the effect of cell type p on cell type q, have the general form:

$$Q^{pq}(\mathbf{d}) = R^{pq} e^{-|\mathbf{d}|/r_{pq}} - A^{pq} e^{-|\mathbf{d}|/a_{pq}}. \tag{10}$$

We list our parameter values for cell migration in Table 2 and provide a qualitative illustration of our cell–cell forces in Fig. 4d. To keep cells in the domain, we specify wall-like boundary conditions on our fin-outline curves (see "Appendix B.2").

Under Mechanism IV in Sect. 2, we test whether M migration is affected by bone rays on the tailfin. Dependent on a switch parameter ζ, we specify that the velocity of the M cell at position $\mathbf{M}_i$ may be projected along its nearest bone ray, as follows:

$$\mathbf{V}_i = -\sum_{j=1, j\neq i}^{N_\mathrm{M}} \nabla Q^{\mathrm{MM}}(\mathbf{M}_j - \mathbf{M}_i) - \sum_{j=1}^{N_\mathrm{X}} \nabla Q^{\mathrm{XM}}(\mathbf{X}_j - \mathbf{M}_i), \tag{11}$$

$$\frac{d\mathbf{M}_i}{dt} = \begin{cases} ||\mathbf{V}_i||\mathbf{b}_i, & \text{if } \sum_{j=1}^{N_\mathrm{X}} \mathbb{1}_{\Omega_{\mathrm{crowd}}^{\mathbf{M}_i}}(\mathbf{X}_j) + \sum_{j=1}^{N_\mathrm{M}} \mathbb{1}_{\Omega_{\mathrm{crowd}}^{\mathbf{M}_i}}(\mathbf{M}_j) < \zeta \\ \mathbf{V}_i, & \text{otherwise} \end{cases}, \tag{12}$$

where $\mathbb{1}_{\Omega_{\mathrm{crowd}}^{\mathbf{M}_i}}(\cdot)$ is the indicator function in Eq. (8) and $\mathbf{b}_i$ is the unit vector in the direction of the bone ray closest to the ith M cell. (We identify the "closest bone ray" using the discretized bone points in Eq. (1). In particular, across the set of 500 discretized points representing each of our 18 bone rays, we define the closest bone to the ith M cell as the index k for which $||\mathbf{M}_i - \mathbf{B}_j^k||$ is smallest.)

The parameter ζ serves as a switch in Eq. (12) that allows us to test Mechanism IV (Sect. 2) in some simulations:

- *Control case (body-model migration)* When $\zeta = -1$ cells (a condition that can never be met), we specify M migration in the same way as in the prior body model (Volkening and Sandstede 2015).
- *Mechanism IV* When $\zeta = 1000$ cells (a value larger than the number of cells that could be present in Ω_{crowd}), we project M movement along bone rays.

As we show in Fig. 4d, we use different parameters for the four potentials in Eqs. (9) and (11). With one exception (Q^{MX}), these potentials are purely repulsive. Following Volkening and Sandstede (2015), we specify that M cells are repelled from both X and other M at short range. Xanthophores, in turn, are repelled from other X cells at short range. This is motivated by in vitro studies (Inaba et al. 2012; Yamanaka and Kondo 2014) showing that M extracted from fins move away from X cells. We also include repulsive interactions between like cells to maintain experimentally measured cell–cell distances (Takahashi and Kondo 2008). Xanthophores extracted from the fins seem to be attracted to M in vitro (Yamanaka and Kondo 2014). When we include this so-called chase-run behavior in our model, we account for it in the same way as in the body model (Volkening and Sandstede 2015): We specify that M cells attract X cells very locally but repel X at short range.

Although Q^{XX}, Q^{MM}, and Q^{XM} describe short-range repulsion in a manner qualitatively similar to Volkening and Sandstede (2015), we adjust the parameters in these potentials in some simulations, as we note in Table 2. We consider two types of simulation: In the first type, all of our parameters are the same as those in Volkening and Sandstede (2015) (with the caveat that we discuss in the caption of Table 2). In the second type, we adjust the parameters slightly from their body equivalents. These adjustments (namely increasing the length scale over which repulsion occurs and reducing its strength) help widen stripes under Mechanism I when skin growth does not stretch cell positions (as it does on the body). Additionally, when testing Mechanisms IV and V, we remove the attractive component of Q^{MX} and instead model X

cells as simply repelled from M. We made this choice to simplify parameter fitting in this first fin model, since it is less clear how changes made to the migration parameters will impact cell movement when interactions are both repulsive and attractive. Importantly, it was shown in Volkening and Sandstede (2015) that removing attraction in Q^{MX} does not strongly impact pattern formation on the body.

3.2.2 Cell Differentiation

For each day of simulated development, we implement $1/\Delta t_{\mathrm{mig,birth}}$ cycles of cell birth, where $\Delta t_{\mathrm{mig,birth}} \leq 1$ day varies in our simulations and is chosen so that cell birth keeps pace with fin growth. For each such cycle, we implement birth by first selecting a number of possible locations randomly in the domain. We then evaluate these locations for birth based on noisy rules. Because the tailfin grows significantly over the developmental period we simulate, we specify that the number of locations selected grows in time. In particular, the initial values of $n_{\mathrm{diff}}^{\mathrm{M}}$ and $n_{\mathrm{diff}}^{\mathrm{X}}$ at 18 dpf vary in our simulations (see "Appendix B.5"), but they both grow by 20 cells each day:

$$N_{\mathrm{diff}}^{\mathrm{M}}(t) = n_{\mathrm{diff}}^{\mathrm{M}} + 20(t-18) = \text{ number of locations evaluated for } M \text{ birth on day } t,$$
$$N_{\mathrm{diff}}^{\mathrm{X}}(t) = n_{\mathrm{diff}}^{\mathrm{X}} + 20(t-18) = \text{ number of locations evaluated for } X \text{ birth on day } t.$$

We describe how we identify possible positions for cell birth within our fin domain in detail in "Appendix B.4." Briefly, we select these positions uniformly at random from a rectangle surrounding the fin, and we then consider only those locations that fall within the fin. Furthermore, under Mechanism V (see Sect. 4.5), we model M cells as arising from precursors on the bone rays. In this case, we choose locations for M birth in association with the coordinates of our discretized bones in Eq. (1).

Our rules for cell birth at randomly selected positions are adapted from the body model (Volkening and Sandstede 2015), and they depend on the proportions of cells in the short- and long-range neighborhoods in Eqs. (4)–(7). In Volkening and Sandstede (2015), a new M cell appears at the selected location $\mathbf{z}$ (if not overcrowded) when there are more M than X in $\Omega_{\mathrm{loc}}^{\mathbf{z}}$ and more X than M in $\Omega_{\mathrm{podia}}^{\mathbf{z}}$. ($X$ birth occurs under the opposite conditions; also see Fig. 4f.) Here, we adjust these base rules to include a switch parameter that allows us to test Mechanism II (the presence of alignment cues from developing body stripes) in some simulations.

We specify that a new X cell appears at the selected location $\mathbf{z} = (z_x, z_y)$ when

$$\Bigg[\Bigg(\underbrace{z_x < d}_{[A]\text{ Mechanism II switch}} \quad \text{and} \quad \underbrace{\sum_{i=1}^{N_{\mathrm{X}}} \mathbb{1}_{\Omega_{\mathrm{rand}}^{\mathbf{z}}}(\mathbf{X}_i) + \sum_{i=1}^{N_{\mathrm{M}}} \mathbb{1}_{\Omega_{\mathrm{rand}}^{\mathbf{z}}}(\mathbf{M}_i) = 0}_{[B]\text{ Mechanism II only impacts birth at low density}}\Bigg)$$
$$\text{or} \quad \underbrace{\sum_{i=1}^{N_{\mathrm{X}}} \mathbb{1}_{\Omega_{\mathrm{loc}}^{\mathbf{z}}}(\mathbf{X}_i) > \phi \sum_{i=1}^{N_{\mathrm{M}}} \mathbb{1}_{\Omega_{\mathrm{loc}}^{\mathbf{z}}}(\mathbf{M}_i)}_{[C]\text{ short-range activation}}\Bigg] \quad \text{and} \quad \underbrace{\sum_{i=1}^{N_{\mathrm{M}}} \mathbb{1}_{\Omega_{\mathrm{podia}}^{\mathbf{z}}}(\mathbf{M}_i) > \psi \sum_{i=1}^{N_{\mathrm{X}}} \mathbb{1}_{\Omega_{\mathrm{podia}}^{\mathbf{z}}}(\mathbf{X}_i)}_{[D]\text{ long-range inhibition}}$$

$$\text{and} \quad \underbrace{\sum_{i=1}^{N_X} \mathbb{1}_{\Omega^{\mathbf{z}}_{\text{crowd}}}(\mathbf{X}_i) + \sum_{i=1}^{N_M} \mathbb{1}_{\Omega^{\mathbf{z}}_{\text{crowd}}}(\mathbf{M}_i) < \kappa}_{[E]\text{ condition to prevent overcrowding}}, \tag{13}$$

where we define the indicator functions $\mathbb{1}_{\Omega^{\mathbf{z}}_{\text{rand}}}(\cdot)$, $\mathbb{1}_{\Omega^{\mathbf{z}}_{\text{loc}}}(\cdot)$, $\mathbb{1}_{\Omega^{\mathbf{z}}_{\text{podia}}}(\cdot)$, and $\mathbb{1}_{\Omega^{\mathbf{z}}_{\text{crowd}}}(\cdot)$ in Eq. (8), and we provide our parameters in Table 3.

Similarly, we add a new M cell to the domain at position $\mathbf{z}$ when

$$\Bigg[\Bigg(\underbrace{z_x < d}_{[A]\text{ Mechanism II switch}} \quad \text{and} \quad \underbrace{\sum_{i=1}^{N_X} \mathbb{1}_{\Omega^{\mathbf{z}}_{\text{rand}}}(\mathbf{X}_i) + \sum_{i=1}^{N_M} \mathbb{1}_{\Omega^{\mathbf{z}}_{\text{rand}}}(\mathbf{M}_i) = 0}_{[B]\text{ Mechanism II only impacts birth at low density}}\Bigg)$$

$$\text{or} \quad \underbrace{\sum_{i=1}^{N_M} \mathbb{1}_{\Omega^{\mathbf{z}}_{\text{loc}}}(\mathbf{M}_i) > \alpha \sum_{i=1}^{N_X} \mathbb{1}_{\Omega^{\mathbf{z}}_{\text{loc}}}(\mathbf{X}_i)}_{[C]\text{ short-range activation}}\Bigg] \quad \text{and} \quad \underbrace{\sum_{i=1}^{N_X} \mathbb{1}_{\Omega^{\mathbf{z}}_{\text{podia}}}(\mathbf{X}_i) > \beta \sum_{i=1}^{N_M} \mathbb{1}_{\Omega^{\mathbf{z}}_{\text{podia}}}(\mathbf{M}_i)}_{[D]\text{ long-range inhibition}}$$

$$\text{and} \quad \underbrace{\sum_{i=1}^{N_X} \mathbb{1}_{\Omega^{\mathbf{z}}_{\text{crowd}}}(\mathbf{X}_i) + \sum_{i=1}^{N_M} \mathbb{1}_{\Omega^{\mathbf{z}}_{\text{crowd}}}(\mathbf{M}_i) < \eta}_{[E]\text{ condition to prevent overcrowding}}. \tag{14}$$

The parameters ϕ, ψ, α, and β in Eqs. (13)–(14) are involved in short-range activation and long-range inhibition; κ and η prevent overcrowding; and d is a switch parameter that allows us to select whether or not to include Mechanism II in a given simulation. We note that ϕ, ψ, α, β, κ, and η take on the same (or slightly altered) values as in the body model (Volkening and Sandstede 2015) (see Table 3). When we alter these parameters, we do so to reduce long-range inhibition and increase short-range activation in cell birth; additionally, we replace η and κ (involved in cell overcrowding) with the values used in the more recent model (Volkening and Sandstede 2018).

Following the example in Volkening and Sandstede (2015), we also include a small amount of random cell birth in some simulations. When included, we model random differentiation in exactly the same way as in the body model (Volkening and Sandstede 2015). For each of the $N^{\text{M}}_{\text{diff}}(t)$ locations $\mathbf{z}$ evaluated for possible M birth at day t, if there are no cells in $\Omega^{\mathbf{z}}_{\text{rand}}$ (a disk of radius 100 μm centered at $\mathbf{z}$), we place a new M cell at $\mathbf{z}$ with probability $p_{\text{M}}\Delta t_{\text{mig,birth}}$. The corresponding rule also applies for X cell birth, with probability $p_{\text{X}}\Delta t_{\text{mig,birth}}$, as in the body model (Volkening and Sandstede 2015).

The conditions in Eqs. (13)–(14) can be expressed as

$$[\ (\ A\ \&\ B\ )\ ||\ C\ ]\ \&\ D\ \&\ E.$$

Adjusting d in Eqs. (13)–(14) then leads to two different dynamics:

– *Control case (body-model birth)* When $d = -1$ μm, Eqs. (13)–(14) reduce to C & D & E, the base rules of short-range activation and long-range inhibition (with overcrowding prevented) used in Volkening and Sandstede (2015).

– *Mechanism II* When $d = 150\,\mu$m in Eqs. (13)–(14), we allow cells to differentiate in a small neighborhood of the proximal edge of the fin (when cell density is low) according to long-range activation alone (see Fig. 4g). This models cells entering the fin from the proximal edge, where the fin connects with the body.

3.2.3 Cell Competition

After cell migration and birth, we evaluate every cell for possible death once on each simulated day of development. Motivated by ablation experiments on the fish body (Nakamasu et al. 2009), we specify short-range competition between M and X. We also include a long-range survival signal from X to M cells: Black cells die with small probability informed by Nakamasu et al. (2009) when there are insufficient X cells present in adjacent interstripes. Our rules are the same as those used in the body model (Volkening and Sandstede 2015), and we reproduce them below:

$$\underbrace{\sum_{i=1}^{N_{\mathrm{X}}} \mathbb{1}_{\Omega_{\mathrm{loc}}^{\mathbf{M}_j}}(\mathbf{X}_i) > \mu \sum_{i=1}^{N_{\mathrm{M}}} \mathbb{1}_{\Omega_{\mathrm{loc}}^{\mathbf{M}_j}}(\mathbf{M}_i)}_{\text{local competition with } X} \quad \text{or} \quad \underbrace{P_i \sum_{i=1}^{N_{\mathrm{M}}} \mathbb{1}_{\Omega_{\mathrm{podia}}^{\mathbf{M}_j}}(\mathbf{M}_i) > \xi \sum_{i=1}^{N_{\mathrm{X}}} \mathbb{1}_{\Omega_{\mathrm{podia}}^{\mathbf{M}_j}}(\mathbf{X}_i)}_{\text{long-range survival signals from } X}$$

$$\Longrightarrow \quad \text{death of } M \text{ cell at } \mathbf{M}_j, \tag{15}$$

$$\underbrace{\sum_{i=1}^{N_{\mathrm{M}}} \mathbb{1}_{\Omega_{\mathrm{loc}}^{\mathbf{X}_j}}(\mathbf{M}_i) > \nu \sum_{i=1}^{N_{\mathrm{X}}} \mathbb{1}_{\Omega_{\mathrm{loc}}^{\mathbf{X}_j}}(\mathbf{X}_i)}_{\text{local competition with } M} \quad \Longrightarrow \quad \text{death of } X \text{ cell at } \mathbf{X}_j, \tag{16}$$

where P_i is a Bernoulli random variable with mean p_{death} based on Nakamasu et al. (2009) and the parameters μ, ξ, and ν are involved in short-range activation and long-range inhibition. We provide our cell death parameters in Table 4 in "Appendix A." The values of ν and p_{death} are the same as in Volkening and Sandstede (2015). In some simulations, we adjust μ and ξ from their body-model equivalents. When we adjust these two parameters, we do so to increase the strength of M and X competition locally. This helps developing stripes (respectively, interstripes) gradually extend from proximal to distal without being interrupted by the appearance of X (respectively, M cells) blocking their path.

3.2.4 A Note on Empirical Similarities on the Fish Body and Tailfin

We actively made the choice to base our fin model on the body model (Volkening and Sandstede 2015) to test whether the same M and X interactions can account for patterning in both regions. Nevertheless, it is worth noting where the rules, that we use, also have a basis in the biological data for fins. First, the rules and parameters for cell birth in Volkening and Sandstede (2015) are heavily based on ablation experiments (Nakamasu et al. 2009) that were performed on the fish body. Ablation severely damages the fins, so the same data are not available for the tailfin (Watanabe and Kondo 2015b). However, experiments with a temperature-sensitive mutation (Parichy

and Turner 2003) have indicated that X support M cells at long range on the fins (Watanabe and Kondo 2015b). Furthermore, Goodrich et al. (1954) provided early evidence for M and X competition, as well as a repulsion of M by X cells on the fins.

4 In Silico Pattern Formation on the Tailfin

We now simulate the agent-based model that we adapted from the body model (Volkening and Sandstede 2015) under the five fin-specific mechanisms identified in Sect. 2, namely:

I Distal epithelial growth (Fig. 4a);
II Alignment cues from body patterns (Fig. 4g);
III Uniform epithelial growth along bone rays (Fig. 4b);
IV Melanophore migration along bone rays (Fig. 4e); and
V Melanophore differentiation in association with bone rays (Fig. 4h).

By testing these different mechanisms, we explore how skin growth, bone rays, and the body–fin interface may affect patterning on the tailfin. Our goal is to help begin to reconcile the differences in pattern dynamics that are present on the fish body and tailfin. Our main result is a demonstration that two cell types can produce horizontal stripes on the caudal fin without iridophores. We find that there are several possible mechanisms that can align stripes, suggesting directions for future work related to pattern robustness.

In this initial modeling study of tailfin patterns, we adopt an exploratory perspective and focus on reproducing macro-scale features (with the exception of measurements in Figs. 6b, 7b). It is important to note that the model (Volkening and Sandstede 2015) on which we base our fin work agrees with several quantitative measurements on the fish body. Future studies can fine-tune parameters and length scales to account for new data on fins. Based on our view of the timelines of wild-type development presented in Parichy et al. (2009), we identify four broad qualitative measurements of model performance. We consider the model successful if (1) horizontal stripes develop; (2) stripes and interstripes form by extending from proximal to distal (Tu and Johnson 2010; Eom et al. 2015); (3) stripes form initially radially, but later adopt a horizontal alignment; and (4) four horizontal stripes are fully formed (e.g., have roughly reached the distal edge of the fin) at stage J++ ($\approx$ 100 dpf). We run many stochastic simulations and seek to meet these conditions consistently.

As the initial condition for our simulations, we start with a pattern that approximates the tailfin at 18 dpf (see "Appendix B.3"). We specify a central M strip and a random distribution of X cells (e.g., see Fig. 5a). We do not include M randomly across the domain, though black cells can be seen dispersed on the fin at the PB stage in images in Parichy et al. (2009). As we discuss in Sect. 5, we assume that these cells are in an earlier, larval form. The works (Tu and Johnson 2010; Rawls and Johnson 2000), for example, mention the presence of several types of M cells on the fin.

4.1 Mechanism I: Distal Epithelial Growth

As an initial test of our model, we simulate patterning under the assumption of distal epithelial growth, so that cell positions remain unaltered during fin growth. Our rules for cell behavior in this setting are the same as those implemented in the body model (Volkening and Sandstede 2015) (e.g., we set the switch parameters in Eqs. (12) and (13)–(14) to $\zeta = -1$ cells and $d = -1\,\mu$m, respectively). As we show in Fig. 5a, epithelial growth at the distal end of the fin does not account for stripe directionality under the body model (Volkening and Sandstede 2015). The strip of M cells in our initial condition at 18 dpf is sufficient to specify stripe alignment proximally, but the dorsal pattern lacks horizontal directionality. This loss of horizontal alignment is not surprising when compared to the ablation experiments (Yamaguchi et al. 2007) simulated in Volkening and Sandstede (2015). In the absence of a pre-pattern in a portion of the domain (whether due to ablation on the fish body or empty space in the fin lobes), stripes form with lost directionality but maintained width.

The fact that the stripes continue to form horizontally near the proximal edge of the fin in Fig. 5a is most likely due to the strip of M cells present in our initial condition in this region. We expect that the horizontal alignment that we observe there is also related to the smaller height of the fin near the proximal edge. Because we only allow random birth at low cell densities, smaller domains reduce the space available for random differentiation to operate and disrupt patterning. The appearance of vertical stripes within the fin lobes is particularly interesting and suggests avenues for future work, as several studies (e.g., Parichy and Turner 2003) have observed vertical stripes in fin experiments.

4.2 Mechanisms I and II: Distal Epithelial Growth with Alignment Cues from the Body

In Fig. 5a, cell differentiation at random locations in the lobes seems to disrupt stripe alignment. We therefore do not include random birth here (e.g., we set $p_M = p_X = 0$). Instead, we include special dynamics in a narrow region near the body–fin interface: We model alignment cues from the body (Mechanism II) by setting $d = 150\,\mu$m in Eqs. (13)–(14). Near the body–fin interface, we then allow cells to be born based on long-range inhibition alone (see Fig. 4g). It is important to note that we cannot remove random birth if we do not implement Mechanism II: Without either random birth or Mechanism II, there would be no new stripes added to our initial condition, as there would be no like cells present locally to activate the new formation of stripes or interstripes [see the form of our conditions in Eqs. (13)–(14)].

Our special condition for cell birth near the body–fin interface (Mechanism II) can be interpreted biologically in two main ways: First, precursors at the body–fin interface could conceivably interact with the developing body pattern. In particular, allowing cells to appear entirely due to long-range signals (without the need for established cells nearby) could model cells differentiating from precursors or existing cells at the body–fin interface. Second, Mechanism II can be viewed as modeling cells entering the fin through migration from the body pattern.

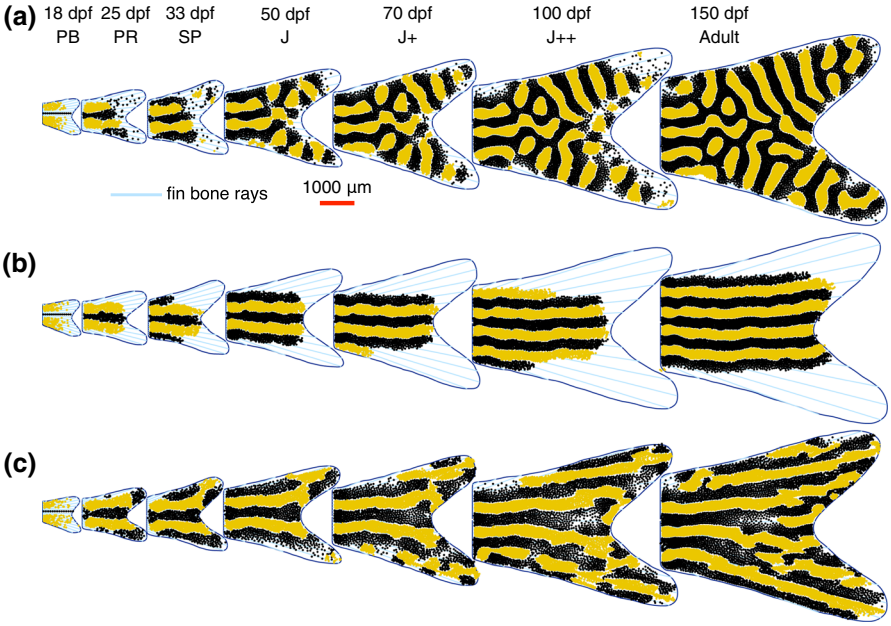

Fig. 5 Simulated pattern formation under Mechanisms I–III. **a** Under Mechanism I, our cell interactions (and the associated parameters) are the same as in the body model (Volkening and Sandstede 2015). We assume skin growth occurs at the distal edge of the fin, so that cell positions are not altered due to domain growth (see Fig. 4a). In this case, random differentiation disrupts pattern alignment. **b** Under Mechanisms I and II, we no longer allow random differentiation, and we instead model cells as interacting with the developing body pattern or precursors at the body–fin interface (see Fig. 4g). To ensure pattern formation keeps pace with growth in this setting, we reduce $\Delta t_{\text{mig, birth}}$, allowing for more frequent cell birth. Notably, Mechanisms I and II together produce patterns that spread from proximal to distal, but the stripes never appear radially as in Fig. 2d. **c** Under uniform epithelial growth with body-alignment cues (Mechanism II and III), we stretch cell positions radially as the fin grows. This mechanism is able to produce aligned stripes, but stripe–interstripe boundaries are tortuous. The red scale bar is 1000 μm and applies to all of the fins in this figure

As we show in Fig. 5b, combining Mechanisms I and II produces straight stripes that form by spreading from proximal to distal across the tailfin. In order to obtain good performance under these mechanisms, we find that it is critical that our time step for cell migration and birth ($\Delta t_{\text{mig,birth}}$) is small and that the number of locations evaluated for M birth is sufficiently large. This ensures that pattern formation keeps pace with fin growth, and it allows stripes to form by the highly controlled addition of pigment cells to the developing patterns. We obtain patterns that are similar to those in Fig. 5b in roughly 65% of 40 stochastic simulations. The most frequent altered patterns feature straight stripes that form at a slight angle away from the horizontal, suggesting that it is not sufficient to rely on highly controlled cell birth to specify horizontal pattern alignment robustly.

4.3 Mechanisms II and III: Uniform Epithelial Growth with Alignment Cues from the Body

Under Mechanism III, we assume that the growing skin on the tailfin stretches across the bone rays, expanding everywhere as additional segments are added to the rays at their distal edges (Goldsmith et al. 2006, 2003). We implement this by scaling cell positions radially as the fin grows (see Fig. 3b, c). As we show in Fig. 5c, uniform growth can account for some stripe directionality. Although our simulations under this mechanism produce aligned stripes, they maintain a strongly radial structure throughout fin development.

It is important to note that, in addition to uniform epithelial growth, we also include both random birth and Mechanism II (alignment cues from the body pattern) in Fig. 5c. If we remove Mechanism II and implement only uniform growth with random birth, we obtain the same qualitative pattern behavior in Fig. 5c (results not shown). In both cases, patterns form very quickly across the fin and maintain a radial nature. We suggest that one could fine-tune our parameters (e.g., particularly those related to cell birth rates) in the future to determine whether uniform epithelial growth can produce more gradual pattern formation across the caudal fin.

4.4 Mechanisms I, III, and IV: *M* Migration Along Bone Rays with Distal Epithelial Growth and Alignment Cues from the Body

Empirical images in Parichy et al. (2009) suggest that M cells appear in close association with the rays. Because the caudal fin is thin in comparison with the fish body, we suggest that it is plausible that the bones on the tailfin physically hamper M movement across rays (Mechanism IV in Sect. 2). For example, in an early study (Goodrich et al. 1954) of the anal fin, M cells were described as invading yellow regions generally along the bone rays. The study (Tu and Johnson 2010) also noted that melanophore clones were distributed parallel to rays on the caudal fin. We implement Mechanism IV by setting the switch parameter ξ to 1000 cells in Eq. (12), so that the velocity of each M cell is projected along its nearest bone ray (also see Fig. 4e).

As we show in Fig. 6a, if we enforce M migration along the rays, our model is able to generate stripe patterns with horizontal alignment. These patterns form by gradually extending distally, and three dark stripes reach the distal end of the fin domain around 100 dpf. Nevertheless, Mechanism IV (together with distal epithelial growth and alignment cues from the body) is not reliable across our stochastic simulations. Based on a visual classification of 50 simulations, we find that roughly 40% of our simulations do not produce horizontal patterns under the assumption of M migration along the rays. The most frequent altered patterns include bent, curved, and wavy stripes (see Fig. 6c, d).

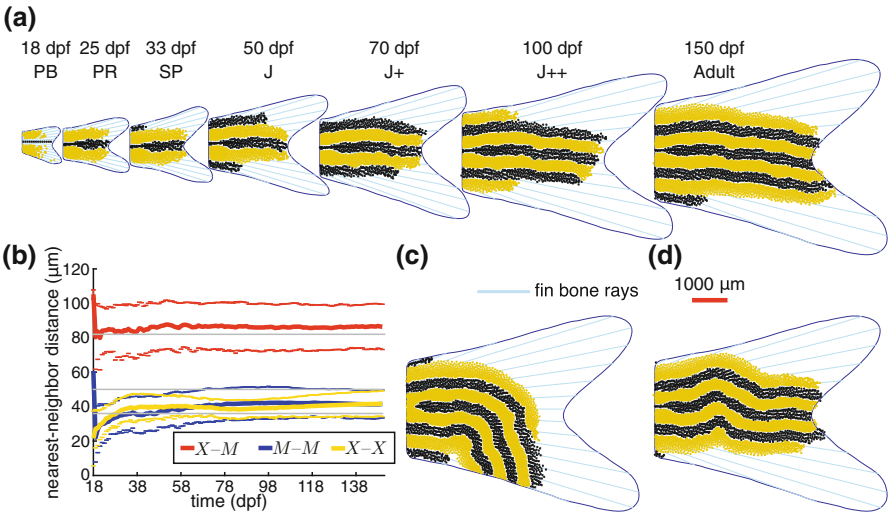

Fig. 6 Examples of simulated pattern formation under the combination of Mechanisms I, III, and IV. **a** Based on early descriptions in Goodrich et al. (1954) and our observations of images in Parichy et al. (2009), bone rays may affect M movement. We implement this by setting $\xi = 1000$ cells in Eq. (12). Here, we show an example of successful pattern formation under Mechanism IV (with distal epithelial growth and alignment cues from the body). We find that projecting M migration along the bones preserves horizontal stripe alignment in roughly 60% of 50 stochastic simulations. **b** The mean nearest-neighbor distances between M cells, between X cells, and between M and X cells at stripe–interstripe boundaries for the simulation in (**a**) are similar to empirical measurements (see "Appendix B.5" for how we calculate these measurements). In grey, we show empirical measurements from Takahashi and Kondo (2008): This study reports that average M–M distances are 50 μm, X–X distances are 36 μm, and X–M distances at stripe–interstripe boundaries are 82 μm. We expect that our M–M distances are smaller because projecting M movement along the rays may remove components of M velocity due to repulsion from other M cells. The dashed curves indicate standard deviation. The most frequent alterations to our target patterns include (**c**) severely curved or bent stripes and **d** wavy stripes (both shown at 150 dpf). The red scale bar is 1000 μm and applies to all of the fins in this figure

4.5 Mechanisms I, III, and V: *M* Birth in Association with Bone Rays with Distal Epithelial Growth and Alignment Cues from the Body

As an alternative means of explaining our observations of M cells in close association with the bones in images of caudal fins from Parichy et al. (2009), it is possible that M cells arise from precursors or other sources that are distributed along or between the rays. [As we mentioned earlier, the study (Tu and Johnson 2010) noted that boundaries of melanophore-clone distributions are parallel to the bones on the tailfin.] To test this hypothesis, we select locations to evaluate for possible M birth along the rays (see "Appendix B.4" for details). As we show in Fig. 7a, requiring that M cells arise along the bones produces patterns that emerge from proximal to distal. Moreover, Mechanism V (with distal epithelial growth and alignment cues from the body) performs robustly across our stochastic simulations, and we show the final patterns that result from a few other representative simulations under this combination of mechanisms in Fig. 7c and d. Although our focus is on qualitative measurements in this first fin model, we

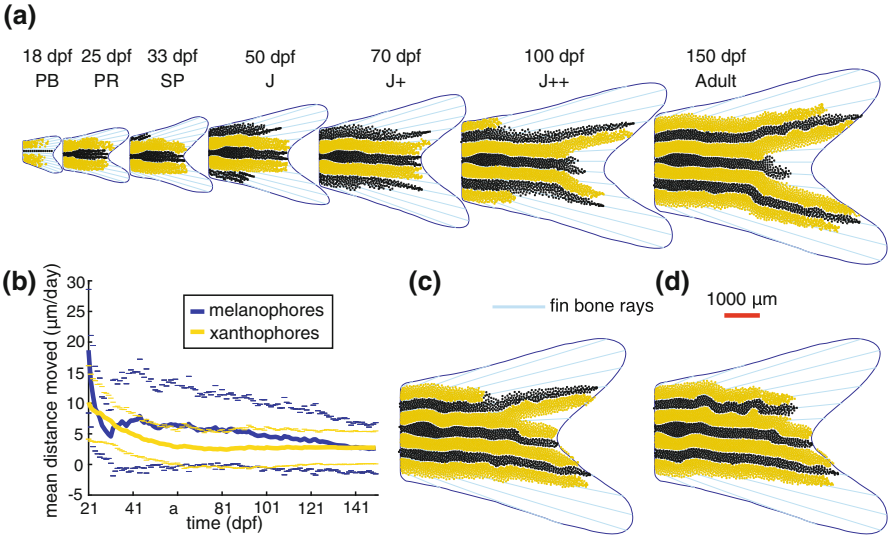

Fig. 7 Simulated pattern formation under the combination of Mechanisms I, III, and V. **a** Based on our observations of images in Parichy et al. (2009), as well as early notes about anal fin patterns in Goodrich et al. (1954), *M* cells seem to appear in close association with bone rays. One explanation (tested in Fig. 6) for this association is that *M* cells migrate along bone rays. Alternatively, it is possible that *M* cells differentiate from precursors associated with the rays (Mechanism V). We find that patterns robustly form by extending distally across the fin under Mechanism V (with distal epithelial growth and alignment cues from the body). **b** The mean distance moved by *M* and *X* cells per day is similar to in vivo (Takahashi and Kondo 2008) and in silico (Volkening and Sandstede 2015) measurements of cell speed. The thick curves indicate the mean distances moved across all the cells on the domain [for the simulation that we present in (**a**)]. The dashed curves indicate standard deviation. See "Appendix B.5" for additional details. **c** Under Mechanism V, patterns often develop with a branched "Y" gap in interstripes or stripes, but we also observe **d** some wavy stripe patterns without such gaps. Patterns in **c** and **d** are at 150 dpf, and the red scale bar (1000 μm) applies to all of the fins in this figure

also show the mean speeds of *M* and *X* cells in time (for the simulation in Fig. 7a) in Fig. 7b. These measurements are similar to empirical estimates (Takahashi and Kondo 2008) that *M* cells move roughly 80–100 μm per week in vivo (e.g., about 11–14 μm per day) when they are active (prior to forming densely packed stripes).

Although the patterns in Fig. 7 form robustly, the stripes that develop under Mechanism V are strongly directed by the radial nature of the bones. This often results in stripes and interstripes that diverge in a "Y" shape at the fin cleft. We suggest that mechanisms of *M* birth may be different in different regions of the fin, as requiring that melanophores are born in association with the bones across the full tailfin in our model produces patterns that too strongly adhere to the radial geometry of the rays.

5 Discussion

In recent years, empirical views of zebrafish skin patterning have changed significantly, as it has become clear that three main types of pigment cells, rather than two, are

necessary for pattern development (Frohnhöfer et al. 2013; Singh et al. 2014; Patterson and Parichy 2013). When iridophores fail to emerge in *shady* mutants (Frohnhöfer et al. 2013; Lopes et al. 2008), dark spots form on the body, but stripe patterns remain intact on the tailfin. Moreover, on the body, the horizontal myoseptum provides an initial source of stripe alignment (Frohnhöfer et al. 2013), but this marker is not present on the caudal fin. To begin to understand these differences between body and fin patterns, we presented an exploratory modeling study of wild-type stripe formation on zebrafish tailfins. We based our agent-based model for melanophore and xanthophore interactions on the prior body model (Volkening and Sandstede 2015), and we traced images of zebrafish from Parichy et al. (2009) to produce growing caudal-fin domains.

We highlighted five different patterning mechanisms that could be at work on the tailfin, and we showed that several of these mechanisms are capable of producing stripes. We find that uniform skin growth can account for radial stripe alignment by stretching pigment cell positions on the fish skin. Under distal epithelial growth, if we incorporate some alignment cues from the developing body stripes into our model indirectly, stripe patterns can form horizontally by progressing from proximal to distal. In our model, pattern robustness under distal epithelial growth depends on melanophore birth keeping pace with fin growth or on bone rays controlling M cell birth or migration. Possibly related, Tu and Johnson (2010) showed that the boundaries of melanophore-clone distributions are parallel to the rays on the tailfin.

Most importantly, our work supports observations related to the *shady* mutant (Frohnhöfer et al. 2013): We find that the interactions of melanophores and xanthophores (without iridophores) can indeed lead to wild-type patterns on the tailfin. We suspect, however, that these cell interactions benefit from external cues (in the form of skin growth, bone rays, the developing body pattern, or other environmental signals), as horizontal-stripe alignment is not robust across our stochastic simulations. We find the most robust results when we assume melanophores arise from precursors associated with the bone rays, but this mechanism also leads to stripe patterns that adhere too closely to the radial nature of the bones. We therefore hypothesize that cues present in the cellular environment may be different in different regions of the fin. For example, it is possible that a cellular signal diffuses from the body–fin interface, that the thickness of the fin affects cell behavior, or that pigment cells are different in different regions of the fin (Tu and Johnson 2010; Rawls and Johnson 2000). As an initial means of accounting for such differences, one could set the switch parameters in Eqs. (12) and (13)–(14) to more moderate values.

Our work provides an initial modeling frame of reference for fin patterning on zebrafish and suggests many places for improvement and extension in future model generations. For example, we focused largely on qualitative measurements, with a particular focus on obtaining horizontal stripe alignment and reproducing proximal-to-distal pattern development. As an additional qualitative measurement, one could seek to reproduce the appearance of random melanophores and xanthophores intermingled in the fin lobes [see images in Parichy et al. (2009) and the supplementary material in Eom et al. (2015)]. However, the short-range melanophore–xanthophore competition in our model does not support this intermingling of unlike cells. We suspect that the cells present in the fin lobes are in an early form and therefore are beyond the scope of a two-cell model. The works (Tu and Johnson 2010; Rawls and Johnson 2000),

for example, mention the presence of several types of melanophores on the fin. In the future, it would be interesting to study how cell stage, age, or lineage impact pattern formation. Finally, comparing quantitative measurements on cell behavior with fin data would be useful in future models, as would large-scale, quantitative studies of in vivo and in silico patterns to more carefully explore pattern robustness and variability. Fin.

Acknowledgements We thank the Nüsslein-Volhard lab for feedback during early model development and are particularly grateful to April Dinwiddie for sharing her expertise on zebrafish fin patterns. We also recognize Emily Briggs, who contributed to earlier discussions on fin growth during an independent study with B.S. and A.V. We thank ICERM for hosting the undergraduate research component of this project.

Compliance with Ethical Standards

Conflict of interest The authors declare that they have no conflict of interest.

A Appendix: Parameters

With the exception of the two switch parameters [namely ζ in Eq. (12) and d in Eqs. (13)–(14)] that we use to implement Mechanism II and IV, we summarize all of the parameters involved in our rules for cell migration, birth, and death in Tables 2, 3, and 4, respectively. We give the simulation-specific values of the switch parameters by figure in "Appendix B.5." We set $d = 150\,\mu\text{m}$ when we include Mechanism II, and we set $\zeta = 1000$ cells when we test Mechanism IV.

B Appendix: Simulation Conditions

We used MATLAB 9.3, The MathWorks, Inc., Natick, MA, USA, to simulate our model of cell interactions on growing fins. Our code is available from the corresponding author on request. We now describe our model implementation ("Appendix B.1"), our boundary conditions ("Appendix B.2"), our initial conditions ("Appendix B.3"), and our methods for selecting cell-birth locations in tailfin domains and implementing Mechanism V ("Appendix B.4"). In "Appendix B.5," we summarize the parameters and simulation conditions associated with our simulations in Figs. 5, 6, and 7.

B.1 Model Implementation

Our simulation begins with an initial condition (see "Appendix B.3") at $t = 18$ dpf. We update cell positions from day t to day $t + 1$ in seven steps:

1. Set the cycle counter c for migration and birth to $c = 1$.
2. Increment $N^{\text{M}}_{\text{diff}}(t)$ and $N^{\text{X}}_{\text{diff}}(t)$ by 20 locations each, so that $N^{\text{M}}_{\text{diff}}(t) = n^{\text{M}}_{\text{diff}} + 20(t - 18)$ locations and $N^{\text{X}}_{\text{diff}}(t) = n^{\text{X}}_{\text{diff}} + 20(t - 18)$ locations.
3. Perform one step $\Delta t_{\text{mig,birth}}$ of migration [e.g., solve Eqs. (9) and (11) using the forward Euler scheme with time step $\Delta t_{\text{mig,birth}}$]. All of our cells migrate simultaneously. We also specify repulsive forces from the discretized fin boundaries at each step $\Delta t_{\text{mig,birth}}$ of migration (see "Appendix B.2").

Table 2 Summary of parameters for cell migration in Eqs. (9)–(12) and (18)

Name	Body-model value	Fin-specific value	Description
$\Delta t_{\text{mig,birth}}$	1 day	1/3 day	Numerical time step for cell migration
R^{MM}	62 μm/day	24.8 μm/day	Melanophore-on-melanophore repulsion
R^{XX}	50 μm/day	20 μm/day	Xanthophore-on-xanthophore repulsion
R^{XM}	137 μm/day	35 μm/day	Xanthophore-on-melanophore repulsion
R^{MX}	113 μm/day	30 μm/day	Melanophore-on-xanthophore repulsion
A^{MX}	163 μm/day	0 μm/day	Melanophore-on-xanthophore attraction
r_{MM}	20 μm	40 μm	Appears in Q^{MM}
r_{XX}	11 μm	31 μm	Appears in Q^{XX}
r_{XM}	20 μm	40 μm	Appears in Q^{XM}
r_{MX}	20 μm	40 μm	Appears in Q^{MX}
a_{MX}	12 μm	40 μm	Appears in Q^{MX}
R^{bnd}	137 μm/day	50 μm/day	Repulsion from the fin boundary
r_{bnd}	20 μm	20 μm	Appears in boundary force potential Q^{bnd}

We note that the model (Volkening and Sandstede 2015) reported $R^{\text{MM}} = 250\,\mu\text{m}$, $R^{\text{XX}} = 200\,\mu\text{m}$, $R^{\text{XM}} = 550\,\mu\text{m}$, $R^{\text{MX}} = 450\,\mu\text{m}$, $A^{\text{MX}} = 650\,\mu\text{m}$, $R^{\text{bnd}} = 137\,\mu\text{m}$, and $\Delta t_{\text{mig}} = 0.25$ days, but these parameters were off by a factor of four; the correct values used in Volkening and Sandstede (2015) are instead $R^{\text{MM}} = 62.5\,\mu\text{m}$, $R^{\text{XX}} = 50\,\mu\text{m}$, $R^{\text{XM}} = 137.5\,\mu\text{m}$, $R^{MX} = 450\,\mu\text{m}$, $A^{\text{MX}} = 162.5\,\mu\text{m}$, $R^{\text{bnd}} = 137.5\,\mu\text{m}$, and $\Delta t_{\text{mig}} = 1$ day. Here, we have rounded the repulsion and attraction parameters down or up to the nearest whole number as indicated

4. Select $N^{\text{M}}_{\text{diff}}(t+1)$ and $N^{\text{X}}_{\text{diff}}(t+1)$ potential locations for M and X birth on the fin domain (outlined by our boundary curve at time $t+1$), respectively. Evaluate these locations (simultaneously) for cell birth based on Eqs. (13)–(14) and random birth if included (e.g., if $p_{\text{M}} > 0$ and $p_{\text{X}} > 0$). Add the newly born cells to the domain at time $t + c\Delta t_{\text{mig,birth}}$.
5. If $c\Delta t_{\text{mig,birth}} = 1$ day, one day of migration and birth has been completed: go to Step 6. Otherwise, increment the cycle counter c for migration and birth ($c = c+1$) and return to Step 3 with the cell positions at time $t + c\Delta t_{\text{mig,birth}}$.
6. Evaluate all of the cells for possible death (simultaneously) through Eqs. (15)–(16). Remove any cells that have died from the domain at day $t+1$. We note that the time step for our cell death rules is always $\Delta t_{\text{death}} = 1$ day.
7. If uniform domain growth is included, scale the cell positions at time $t+1$ using the fin domains and bone rays at times $t+1$ and $t+2$ days as we describe in Sect. 3.1. If distal epithelial growth is included, do not scale the cell positions. The result of this process is the updated cell positions at time $t+1$ days.

B.2 Boundary Conditions

To help keep cells in the fin domain, we include wall-like boundary conditions. For each simulated day t, we discretize the associated fin boundary curve at time t into 500 points: $\{\mathbf{F}_i(t)\}_{i=1,\ldots,500}$. We then specify repulsive forces from these boundary

Table 3 Summary of our parameters for cell birth [see Eqs. (13)–(14)] and model length scales

Name	Body-model value	Fin-specific value	Description
$\Delta t_{\text{mig,birth}}$	1 day	1/3 day	Numerical time step for birth and migration
$n_{\text{diff}}^{\text{M}}$	Varies	600 locations	Initial condition for number of locations selected for possible M differentiation per $\Delta t_{\text{mig,birth}}$ days
$n_{\text{diff}}^{\text{X}}$	Varies	600 locations	Initial condition for number of locations selected for possible X differentiation per $\Delta t_{\text{mig,birth}}$ days
d_{loc}	75 μm	82 μm	Radius of short-range interaction disk Ω_{loc}
d_{crowd}	82 μm	82 μm	Radius of overcrowding disk Ω_{crowd}
d_{rand}	100 μm	100 μm	Radius of disk for random birth Ω_{rand}
d_{podia}	318 μm	318 μm	Inner radius of long-range annulus Ω_{podia}
w_{podia}	25 μm	25 μm	Width of long-range annulus Ω_{podia}
α	1	0.5	Lower bound on $\frac{\sum_{i=1}^{N_{\text{M}}} \mathbf{M}_i}{\sum_{i=1}^{N_{\text{X}}} \mathbf{X}_i}\|_{\Omega_{\text{loc}}}$ for M birth
β	3.5	2.5	Lower bound on $\frac{\sum_{i=1}^{N_{\text{X}}} \mathbf{X}_i}{\sum_{i=1}^{N_{\text{M}}} \mathbf{M}_i}\|_{\Omega_{\text{podia}}}$ for M birth
η	6	4	Upper bound on $(\sum_{i=1}^{N_{\text{M}}} \mathbf{M}_i + \sum_{i=1}^{N_{\text{X}}} \mathbf{X}_i)\|_{\Omega_{\text{crowd}}}$ for M birth
ϕ	1.3	1.3	Lower bound on $\frac{\sum_{i=1}^{N_{\text{X}}} \mathbf{X}_i}{\sum_{i=1}^{N_{\text{M}}} \mathbf{M}_i}\|_{\Omega_{\text{loc}}}$ for X birth
ψ	1.2	1	Lower bound on $\frac{\sum_{i=1}^{N_{\text{M}}} \mathbf{M}_i}{\sum_{i=1}^{N_{\text{X}}} \mathbf{X}_i}\|_{\Omega_{\text{podia}}}$ for X birth
κ	10	6	Upper bound on $(\sum_{i=1}^{N_{\text{M}}} \mathbf{M}_i + \sum_{i=1}^{N_{\text{X}}} \mathbf{X}_i)\|_{\Omega_{\text{crowd}}}$ for X birth
p_{M}	0.03	0	Probability of random M birth per day
p_{X}	0.005	0	Probability of random X birth per day

In "Appendix B.5," we note whether we use the body-model or fin-specific values to produce each figure in the manuscript. Body-model values refer to the parameters used in the prior body model (Volkening and Sandstede 2015)

Table 4 Summary of our parameters for cell death in Eqs. (15)–(16)

Name	Body-model value	Fin-specific value	Description
Δt_{death}	1 day	1 day	Numerical time step for cell death
μ	1	2	Lower bound on $\frac{\sum_{i=1}^{N_X} \mathbf{X}_i}{\sum_{i=1}^{N_M} \mathbf{M}_i}\|_{\Omega_{\text{loc}}}$ for M death
ν	1	1	Lower bound on $\frac{\sum_{i=1}^{N_M} \mathbf{M}_i}{\sum_{i=1}^{N_X} \mathbf{X}_i}\|_{\Omega_{\text{loc}}}$ for X death
ξ	1.2	1.7	Lower bound on $\frac{\sum_{i=1}^{N_M} \mathbf{M}_i}{\sum_{i=1}^{N_X} \mathbf{X}_i}\|_{\Omega_{\text{podia}}}$ for M death
p_{death}	0.0333	0.0333	Probability of M death per day due to long-range effects

In "Appendix B.5," we note whether we use the body-model or fin-specific values to produce each figure in the manuscript. Body-model values refer to the parameter values used in Volkening and Sandstede (2015) to simulate patterning on the zebrafish body

points to our cell agents at each time step of migration $\Delta t_{\text{mig,birth}}$:

$$\text{boundary force on } i\text{th cell at position } \mathbf{C}_i = -\sum_{j=1}^{500} \nabla Q^{\text{bnd}}(\mathbf{F}_j - \mathbf{C}_i) \tag{17}$$

where $\mathbf{C} \in \{\mathbf{M}, \mathbf{X}\}$ and

$$Q^{\text{bnd}}(\mathbf{d}) = R^{\text{bnd}} e^{-|\mathbf{d}|/r_{\text{bnd}}}. \tag{18}$$

These rules are an approximation of Neumann boundary conditions, and we note that a small number of cells escape from our domain in some simulations. Cells are more likely to escape with increasing time, suggesting that it may be useful for future work to increase the number of boundary agents as the fin grows. When cells escape, we remove them from our final simulated images in post-processing.

B.3 Initial Condition

The initial condition for our simulations is motivated by images in Parichy et al. (2009). First, we specify a single horizontal strip of M cells (separated 30 μm apart) at the center of our fin domain (e.g., with y-coordinate 0). Second, for X cells, we consider a random distribution of cells that are concentrated more highly toward the proximal edge of the fin. We choose the y-coordinates of these positions by selecting 500 points uniformly at random between the maximum and minimum y-coordinates for the discretized boundary curve that represents our initial domain at 18 dpf (see "Appendix B.2"). We choose the x-coordinates for these points by taking the absolute value of 500 points sampled from a normal distribution with mean 0 and standard deviation $\sigma = 0.25 x_{\max}(t)$, where $x_{\max}(t)$ is the maximum x-coordinate for our discretized boundary curve at 18 dpf.

As the penultimate step in setting our initial condition, we remove any M or X cells that fall within 25 μm of our discretized boundary curve in Eq. (18). Finally, if more than 300 of our selected X locations fall in the domain, we use only the first 300 such locations in our initial condition.

For the special case of Fig. 5c, after specifying our initial condition as above, we scale the cell positions to account for one day of uniform epithelial growth (for details on how we implement domain growth, see Sect. 3.1). We use these scaled cell positions as our initial condition for the simulations in Fig. 5c.

B.4 Selecting Cell Birth Locations

We consider two methods for selecting $N_{\text{diff}}^{\text{M}}(t)$ possible locations for M birth:

- *Control case (similar to body-model birth)* We choose $2 \times N_{\text{diff}}^{\text{M}}(t)$ locations uniformly at random in a rectangular region surrounding the fin, and we evaluate the first $N_{\text{diff}}^{\text{M}}(t)$ of these positions that are inside the fin domain for possible birth simultaneously.
- *Mechanism V* Under Mechanism V, we first choose $N_{\text{diff}}^{\text{M}}(t)$ points uniformly at random from our discretized bone rays, namely $\{\mathbf{B}_i^j\}$ in Eq. (1). For each such point $\mathbf{B}_k$, we then choose a corresponding location to evaluate for M birth by selecting a point uniformly at random in a ball of radius $r \sim \mathcal{N}(0, 2)$ μm around $\mathbf{B}_k$.

We always select potential X birth locations in the same way as in the M control case.

Lastly, prior to applying our rules for cell birth to the locations that we randomly selected as we outlined above, we require that these positions are strictly greater than 25 μm away from our discretized boundary curve [see Eq. (17) in "Appendix B.2"]. If a randomly selected location is within 25 μm of a discretized boundary point in $\{\mathbf{F}_i(t)\}_{i=1,\ldots,500}$, we do not allow cell birth to occur at that location.

B.5 Instructions for Reproducing Our Figures

We summarize the parameters for our simulated patterns in Figs. 5, 6, and 7 below:

- Figure 5a, Mechanism I (distal epithelial growth)
  - Cell migration: We use the body-model values in Table 2.
  - Cell birth: We use the body-model values in Table 3 with $n_{\text{diff}}^{\text{M}} = n_{\text{diff}}^{\text{X}} = 600$ locations.
  - Cell death: We use the body-model values in Table 4.
  - Skin growth: We do not scale cell positions with domain growth.
  - Switch parameters: In Eq. (12), we use $\zeta = -1$ cells. In Eqs. (13)–(14), we use $d = -1$ μm.
- Figure 5b, Mechanisms I and III (distal epithelial growth with alignment cues from the body)
  - Cell migration: We use the body-model values in Table 2 with one exception: $\Delta t_{\text{mig,birth}} = 0.25$ days (more frequent cell birth and migration than we use in Fig. 5a).

  - Cell birth: We use the body-model values in Table 3 with three exceptions: $\Delta t_{\mathrm{mig,birth}} = 0.25$ days, $p_{\mathrm{M}} = 0$, and $p_{\mathrm{X}} = 0$ (no random birth). We use $n_{\mathrm{diff}}^{\mathrm{M}} = n_{\mathrm{diff}}^{\mathrm{X}} = 600$ locations.
  - Cell death: We use the body-model values in Table 4.
  - Skin growth: We do not scale cell positions with domain growth.
  - Switch parameters: In Eq. (12), we use $\zeta = -1$ cells. In Eqs. (13)–(14), we use $d = 150\,\mu$m (special body–fin interface dynamics; see Fig. 4g).

- Figure 5c, Mechanisms II and III (uniform epithelial growth with alignment cues from the body)
  - Cell migration: We use the body-model values in Table 2.
  - Cell birth: We use the body-model values in Table 3 with $n_{\mathrm{diff}}^{\mathrm{M}} = 1200$ and $n_{\mathrm{diff}}^{\mathrm{X}} = 600$ locations.
  - Cell death: We use the body-model values in Table 4.
  - Skin growth: We scale cell positions along the bone rays with fin growth as we describe in Sect. 3.1.
  - Switch parameters: In Eq. (12), we use $\zeta = -1$ cells. In Eqs. (13)–(14), we use $d = 150\,\mu$m.

- Figure 6, Mechanisms I, III, and IV (M migration along bone rays with alignment cues from the body and distal epithelial growth)
  - Cell migration: We use the fin-specific values in Table 2.
  - Cell birth: We use the fin-specific values in Table 3.
  - Cell death: We use the fin-specific values in Table 4.
  - Skin growth: We do not scale cell positions with domain growth.
  - Switch parameters: In Eq. (12), we use $\zeta = 1000$ cells (so that M movement is always projected along the bones). In Eqs. (13)–(14), we use $d = 150\,\mu$m.
  - Additional note in Fig. 6b: When we calculate the nearest-neighbor distances between cells, we only consider M–M and X–X distances that are less than $200\,\mu$m (this ensures that cells that have escaped our fin domain or appear at low density do not affect our measurements of cell–cell distances in developing stripes). When we calculate M–X distances at stripe–interstripe boundaries, we only consider measurements that are less than $110\,\mu$m. We made this choice so that our M–X distances measure stripe–interstripe separation (in comparison, Takahashi and Kondo (2008) showed that M and X cells are roughly $82\,\mu$m apart at stripe–interstripe boundaries).

- Figure 7, Mechanisms I, III, and V (M birth in association with bone rays, with alignment cues from the body and distal epithelial growth)
  - Cell migration: We use the fin-specific values in Table 2.
  - Cell birth: We use the fin-specific values in Table 3. Additionally, we select locations for cell birth using the coordinates of the discretized bone rays in Eq. (1) (see "Appendix B.4" for details).
  - Cell death: We use the fin-specific values in Table 4.
  - Skin growth: We do not scale cell positions with domain growth.

– Switch parameters: In Eq. (12), we use $\zeta = -1$ cells. In Eqs. (13)–(14), we use $d = 150\,\mu$m.
– Additional note in Fig. 7b: To calculate the distances that cells move per day, we consider the differences in their locations between consecutive days. In particular, the distance the ith M cell moves in one day is $||\mathbf{M}_i(t) - \mathbf{M}_i(t + \Delta t_{\text{mig,birth}})|| + ||\mathbf{M}_i(t + \Delta t_{\text{mig,birth}}) - \mathbf{M}_i(t + 2\Delta t_{\text{mig,birth}})|| + ||\mathbf{M}_i(t + 2\Delta t_{\text{mig,birth}}) - \mathbf{M}_i(t + 1)||$, since $\Delta t_{\text{mig,birth}} = 1/3$ days in this simulation. If a new cell is born at position $\mathbf{M}_j$ at, for example, time $t + \Delta t_{\text{mig,birth}}$, then we define the distance that cell agent moved between day t and day $t + 1$ as just $||\mathbf{M}_j(t + \Delta t_{\text{mig,birth}}) - \mathbf{M}_j(t + 2\Delta t_{\text{mig,birth}})|| + ||\mathbf{M}_j(t + 2\Delta t_{\text{mig,birth}}) - \mathbf{M}_j(t + 1)||$.

References

Bloomfield JM, Painter KJ, Sherratt JA (2011) How does cellular contact affect differentiation mediated pattern formation? Bull Math Biol 73(7):1529–1558

Bullara D, De Decker Y (2015) Pigment cell movement is not required for generation of Turing patterns in zebrafish skin. Nat Commun 6:6971

Caicedo-Carvajal CE, Shinbrot T (2008) In silico zebrafish pattern formation. Dev Biol 315(2):397–403

Eom DS, Inoue S, Patterson LB, Gordon TN, Slingwine R, Kondo S, Watanabe M, Parichy DM (2012) Melanophore migration and survival during zebrafish adult pigment stripe development require the immunoglobulin superfamily adhesion molecule Igsf11. PLoS Genet 8(8):e1002899

Eom DS, Bain EJ, Patterson LB, Grout ME, Parichy DM (2015) Long-distance communication by specialized cellular projections during pigment pattern development and evolution. eLife 4:e12401

Fadeev A, Krauss J, Frohnhöfer HG, Irion U, Nüsslein-Volhard C (2015) Tight junction protein 1a regulates pigment cell organisation during zebrafish colour patterning. eLife 4:e06545

Frohnhöfer HG, Krauss J, Maischein H-M, Nüsslein-Volhard C (2013) Iridophores and their interactions with other chromatophores are required for stripe formation in zebrafish. Development 140(14):2997–3007

Gaffney EA, Lee SS (2015) The sensitivity of Turing self-organization to biological feedback delays: 2d models of fish pigmentation. Math Med Biol 32(1):57–79

Gierer A, Meinhardt H (1972) A theory of biological pattern formation. Kybernetik 12(1):30–39

Goldsmith MI, Fisher S, Waterman R, Johnson SL (2003) Saltatory control of isometric growth in the zebrafish caudal fin is disrupted in *long fin* and *rapunzel* mutants. Dev Biol 259(2):303–317

Goldsmith MI, Iovine MK, O'Reilly-Pol T, Johnson SL (2006) A developmental transition in growth control during zebrafish caudal fin development. Dev Biol 296(2):450–457

Goodrich HB, Nichols R (1931) The development and the regeneration of the color pattern in brachydanio rerio. J Morphol 52(2):513–523

Goodrich HB, Marzullo CM, Bronson WR (1954) An analysis of the formation of color patterns in two fresh-water fish. J Exp Zool 125(3):487–505

Hamada H, Watanabe M, Lau HE, Nishida T, Hasegawa T, Parichy DM, Kondo S (2014) Involvement of Delta/Notch signaling in zebrafish adult pigment stripe patterning. Development 141(2):318–324

Hirata M, Nakamura K-I, Kondo S (2005) Pigment cell distributions in different tissues of the zebrafish, with special reference to the striped pigment pattern. Dev Dyn 234(2):293–300

Inaba M, Yamanaka H, Kondo S (2012) Pigment pattern formation by contact-dependent depolarization. Science 335(6069):677–677

Inoue S, Kondo S, Parichy DM, Watanabe M (2014) Tetraspanin 3c requirement for pigment cell interactions and boundary formation in zebrafish adult pigment stripes. Pigment Cell Melanoma Res 27(2):190–200

Iovine MK (2007) Conserved mechanisms regulate outgrowth in zebrafish fins. Nat Chem Biol 3(10):613–618

Iovine MK, Johnson SL (2000) Genetic analysis of isometric growth control mechanisms in the zebrafish caudal fin. Genetics 155(3):1321–1329

Iwashita M, Watanabe M, Ishii M, Chen T, Johnson SL, Kurachi Y, Okada N, Kondo S (2006) Pigment pattern in *jaguar/obelix* zebrafish is caused by a kir7.1 mutation: implications for the regulation of melanosome movement. PLoS Genet 2(11):e197

Kizil C, Otto GW, Geisler R, Nüsslein-Volhard C, Antos CL (2009) *Simplet* controls cell proliferation and gene transcription during zebrafish caudal fin regeneration. Dev Biol 325(2):329–340

Kondo S, Watanabe M (2015) Black, yellow, or silver: which one leads skin pattern formation? Pigment Cell Melanoma Res 28(1):2–4

Lopes SS, Yang X, Müller J, Carney TJ, McAdow AR, Rauch G, Jacoby AS, Hurst LD, Delfino-Machín M, Haffter P, Geisler R, Johnson SL, Ward A, Kelsh RN (2008) Leukocyte tyrosine kinase functions in pigment cell development. PLoS Genet 4(3):1–13

Mahalwar P, Walderich B, Singh AP, Nüsslein-Volhard C (2014) Local reorganization of xanthophores fine-tunes and colors the striped pattern of zebrafish. Science 345(6202):1362–1364

Mahalwar P, Singh AP, Fadeev A, Nüsslein-Volhard C, Irion U (2016) Heterotypic interactions regulate cell shape and density during color pattern formation in zebrafish. Biol Open 5(11):1680–1690

McMenamin SK, Chandless MN, Parichy DM (2016) Working with zebrafish at postembryonic stages. Methods Cell Biol 134:587–607

Mellgren EM, Johnson SL (2006) *Pyewacket*, a new zebrafish fin pigment pattern mutant. Pigment Cell Res 19(3):232–238

Mills MG, Nuckels RJ, Parichy DM (2007) Deconstructing evolution of adult phenotypes: genetic analyses of *kit* reveal homology and evolutionary novelty during adult pigment pattern development of *Danio* fishes. Development 134(6):1081–1090

Moreira J, Deutsch A (2005) Pigment pattern formation in zebrafish during late larval stages: a model based on local interactions. Dev Dyn 232(1):33–42

Nakamasu A, Takahashi G, Kanbe A, Kondo S (2009) Interactions between zebrafish pigment cells responsible for the generation of Turing patterns. Proc Natl Acad Sci USA 106(21):8429–8434

Nüsslein-Volhard C, Singh AP (2017) How fish color their skin: a paradigm for development and evolution of adult patterns. BioEssays 39(3):1600231

Painter KJ, Bloomfield JM, Sherratt JA, Gerisch A (2015) A nonlocal model for contact attraction and repulsion in heterogeneous cell populations. Bull Math Biol 77(6):1132–1165

Parichy DM, Spiewak JE (2015) Origins of adult pigmentation: diversity in pigment stem cell lineages and implications for pattern evolution. Pigment Cell Melanoma Res 28(1):31–50

Parichy DM, Turner JM (2003) Temporal and cellular requirements for Fms signaling during zebrafish adult pigment pattern development. Development 130(5):817–833

Parichy DM, Elizondo MR, Mills MG, Gordon TN, Engeszer RE (2009) Normal table of postembryonic zebrafish development: staging by externally visible anatomy of the living fish. Dev Dyn 238(12):2975–3015

Patterson LB, Parichy DM (2013) Interactions with iridophores and the tissue environment required for patterning melanophores and xanthophores during zebrafish adult pigment stripe formation. PLoS Genet 9(5):e1003561

Patterson LB, Bain EJ, Parichy DM (2014) Pigment cell interactions and differential xanthophore recruitment underlying zebrafish stripe reiteration and *Danio* pattern evolution. Nat Commun 5:5299

Pfefferli C, Jaźwińska A (2015) The art of fin regeneration in zebrafish. Regeneration 2(2):72–83

Quigley IK, Manuel JL, Roberts RA, Nuckels RJ, Herrington ER, MacDonald EL, Parichy DM (2005) Evolutionary diversification of pigment pattern in *Danio* fishes: differential *fms* dependence and stripe loss in *D. albolineatus*. Development 132(1):89–104

Rawls JF, Johnson SL (2000) Zebrafish *kit* mutation reveals primary and secondary regulation of melanocyte development during fin stripe regeneration. Development 127(17):3715–3724

Rolland-Lagan A-G, Paquette M, Tweedle V, Akimenko M-A (2012) Morphogen-based simulation model of ray growth and joint patterning during fin development and regeneration. Development 139(6):1188–1197

Singh AP, Nüsslein-Volhard C (2015) Zebrafish stripes as a model for vertebrate colour pattern formation. Curr Biol 25(2):R81–R92

Singh AP, Schach U, Nüsslein-Volhard C (2014) Proliferation, dispersal and patterned aggregation of iridophores in the skin prefigure striped colouration of zebrafish. Nat Cell Biol 16(6):604–611

Singh AP, Frohnhöfer H-G, Irion U, Nüsslein-Volhard C (2015) Response to comment on "Local reorganization of xanthophores fine-tunes and colors the striped pattern of zebrafish". Science 348(6232):297–297

Takahashi G, Kondo S (2008) Melanophores in the stripes of adult zebrafish do not have the nature to gather, but disperse when they have the space to move. Pigment Cell Melanoma Res 21(6):677–686

Tu S, Johnson SL (2010) Clonal analyses reveal roles of organ founding stem cells, melanocyte stem cells and melanoblasts in establishment, growth and regeneration of the adult zebrafish fin. Development 137(23):3931–3939

Tu S, Johnson SL (2011) Fate restriction in the growing and regenerating zebrafish fin. Dev Cell 20(5):725–732

Turing AM (1952) The chemical basis of morphogenesis. Philos Trans R Soc Lond B Biol Sci 237(641):37–72

Volkening A, Sandstede B (2015) Modelling stripe formation in zebrafish: an agent-based approach. J R Soc Interface 12(112):20150812

Volkening A, Sandstede B (2018) Iridophores as a source of robustness in zebrafish stripes and variability in *Danio* patterns. Nat Commun 9:3231

Walderich B, Singh AP, Mahalwar P, Nüsslein-Volhard C (2016) Homotypic cell competition regulates proliferation and tiling of zebrafish pigment cells during colour pattern formation. Nat Commun 7:11462

Watanabe M, Kondo S (2015a) Comment on "Local reorganization of xanthophores fine-tunes and colors the striped pattern of zebrafish". Science 348(6232):297–297

Watanabe M, Kondo S (2015b) Is pigment patterning in fish skin determined by the Turing mechanism? Trends Genet 31(2):88–96

Watanabe M, Sawada R, Aramaki T, Skerrett IM, Kondo S (2016) The physiological characterization of connexin41.8 and connexin39.4, which are involved in the striped pattern formation of zebrafish. J Biol Chem 291(3):1053–1063

Woolley TE, Maini PK, Gaffney EA (2014) Is pigment cell pattern formation in zebrafish a game of cops and robbers? Pigment Cell Melanoma Res 27(5):686–687

Yamaguchi M, Yoshimoto E, Kondo S (2007) Pattern regulation in the stripe of zebrafish suggests an underlying dynamic and autonomous mechanism. Proc Natl Acad Sci USA 104(12):4790–4793

Yamanaka H, Kondo S (2014) In vitro analysis suggests that difference in cell movement during direct interaction can generate various pigment patterns in vivo. Proc Natl Acad Sci USA 111(5):1867–1872